



# Experimental observations of 3D flow alterations by vegetation under oscillatory flows

Jorge E. San Juan<sup>1</sup> · Gerardo Veliz Carrillo<sup>2</sup> · Rafael O. Tinoco<sup>1</sup>

Received: 10 August 2018 / Accepted: 21 February 2019 / Published online: 2 March 2019  
© Springer Nature B.V. 2019

## Abstract

This study presents observations from a series of experiments on an oscillatory tunnel, using a three-dimensional, volumetric particle image velocimetry system to investigate the effect of a single plant morphology on flow alterations. Three synthetic plants, mimicking three species representative of riverine, tidal, and coastal vegetation communities are investigated under various combinations of wave period and orbital excursion. The study allows to investigate the temporal and spatial distribution of the velocity field past the submerged plants with high spatial resolution. It shows that even a detailed characterization of plant morphology, represented by obstructed area or patch porosity, is not enough to accurately parameterize variations in instantaneous velocity, turbulent kinetic energy, bed shear stresses, and coherent flow structures. The study shows that bending and swaying of the plant generates eddies at multiple scales, at various locations and orientations with respect to the stem, branches, and leaves, which may be overlooked with point measurements or even 2D PIV, and can significantly enhance or dampen forces at the bed driving sediment transport processes in sparse vegetation patches.

**Keywords** Vegetation · Oscillatory flow · Volumetric PIV · Turbulence · Bed shear stress

## 1 Introduction

Restoration and conservation for aquatic ecosystems exposed to wave action rely on accurate understanding of aquatic vegetation—flow interactions [20, 27]. Such interactions impact ecosystems directly and indirectly through various mechanisms. For example, turbulence levels inside and around vegetated patches determine erosion/deposition patterns [61, 62], while sediment transport affects water quality and physicochemical characteristics of the substrata. These dynamics impact biota and alter ecological functions [35]. In consequence, relationships among biotic and abiotic components of aquatic ecosystems challenge restoration and conservation efforts [8, 45]. Temporal and spatial variability also

---

✉ Jorge E. San Juan  
snjnbln2@illinois.edu

<sup>1</sup> Ven Te Chow Hydrosystem Laboratory, Department of Civil and Environmental Engineering, University of Illinois at Urbana-Champaign, Urbana, IL, USA

<sup>2</sup> Department of Civil and Environmental Engineering, University of California, Berkeley, CA, USA

adds complexity of these processes in habitats subject to oscillatory flows, such as estuaries, nearshore, and offshore regions [19, 24].

Plant morphology, defined as the spatial distribution of biomass and geometric features [4], differs from simplified shapes in nature. Morphological structures (leaves, branches, stems) impose heterogeneous resistance upon the flow in terms of irregular blockage and biomechanical resistance [49] altering flow organization and turbulence statistics. For example, Albayrak et al. [5] found that turbulence scales are strongly associated with morphological structures of the plant and its biomechanical properties. Parameters such as frontal area, volumetric biomass, number of shoots per plane area, mean stem-to-stem separation, flexibility, and submergence, allow for characterization of plant morphology in context of vegetation—flow interactions [4, 40, 42]. Velocity fields, drag, and turbulence structure become highly affected by these morphological parameters. Vertical velocity gradients and vertical secondary flows develop as a consequence of vegetation obstruction. Vegetation density and distribution define strength, degree of velocity inflection, and spatial heterogeneity of velocity fields [12, 31, 34]. Drag varies across morphological scales: leaves, stems, shoots, and vegetated patches [5, 56, 63]. Henry et al. [19] point out that understanding reciprocity between complexity of biomorphological features and flow is a key factor to accurately represent drag. Vegetation density, plant flexibility, and submergence, determine levels of turbulence inside and around the canopy [46, 53]. The combination of hydraulic and canopy morphology determines wake-turbulence production near the bed, affecting deposition/erosion rates within and around the patch. Balance between vegetation-drag and shear flow above the canopy varies significantly between rigid and flexible vegetation and defines in-canopy turbulence [52, 55]. As flexible vegetation aligns with the flow and reduces vegetation-drag, they allow higher in-canopy velocity and hence higher wake-production near the bed [2]. Furthermore, solid volume fraction and submergence influence vertical and horizontal distribution of turbulent kinetic energy, as the flow becomes highly three-dimensional. Zhang et al. [71] found that near-bed turbulence increases with volumetric solid fraction in oscillatory flows when wave excursion-to-plant spacing ratio is greater than 0.5. Because emergent canopies span across the whole flow depth, they transform wave-scale turbulence into stem-scale turbulence as the waves travel through [52], developing a nonuniform spatial turbulence distribution in the direction of the traveling waves [60]. On the other hand, studies like Ghisalberti and Schlosser [14] and Abdolahpour et al. [1], show that submerged canopies produce flow structure and turbulence variability characterized by above-canopy, shear, and in-canopy flow. Plant morphology thus clearly becomes a valuable component to understand vegetation—hydrodynamic interactions and their implications in their ecosystem.

Even though aquatic vegetation develops three-dimensional flow features inside and around the canopy, most studies in oscillatory flows over vegetated beds rely on point-wise and two-dimensional approaches. Computational cost of 3D modeling and instrument capabilities limit detailed analysis of instantaneous three-dimensional velocity fields. Current 1D and 2D experimental approaches have been useful to investigate certain processes: flow resistance, wave attenuation and energy dissipation. For instance, Acoustic Doppler Velocimeters (ADV) have been extensively used to study flow structure, turbulence, and wave attenuation in laboratory settings [3, 53] and field studies [40, 54] in combination with sediment transport estimation [55, 65]; and arrays of single-point gauge for water surface elevation [6, 30, 67]. On the other hand, studies like Tinoco and Cowen [63] and Hansen and Reinderbach [17] have implemented Particle Image Velocimetry (PIV) as a two-dimensional approach to characterize hydrodynamic response under different morphological characteristics, in laboratory and field, respectively, which allows to capture certain

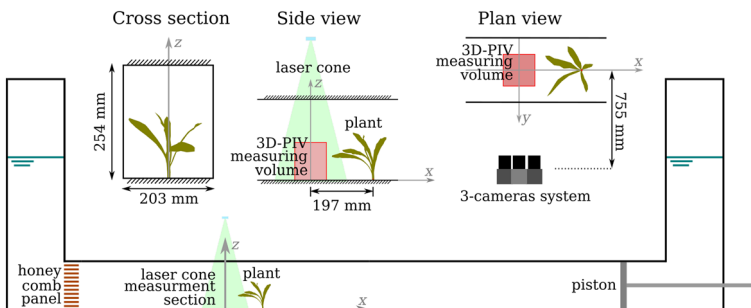
flow structures when lateral uniformity can be relatively ensured [14]. Due to the limitation of 3D experimental data availability, even three-dimensional numerical simulation depends on point-wise measurements for calibration and validation. For example, Maza et al. [36, 37] studied wave attenuation and propagation using 3D simulations, validating their models using water surface gauge from experiments. Capturing three dimensionality of vegetated flows under oscillatory conditions is thus needed to better understand these complex vegetation—hydrodynamic interactions [10, 29].

Simplified models allow us to efficiently evaluate the role of specific vegetation parameters in flow-canopy interactions. Studies like Luhar and Nepf [32], Garcia and Lopez. [12], and Nepf [41] have contributed to the fundamental understanding of these interactions. Unfortunately, oversimplification may misrepresent spatial organization of the flow, wake development [7], and lead to underestimation of sediment transport rates [22]. Accurate representation and quantification of plant morphology is important to accurately simulate flow velocity, sediment transport, and drag forces for specific species. To improve our understanding of flow-vegetation interaction for complex plant morphologies under oscillatory flows, we investigate experimentally how vegetation morphology of a single plant affects flow structure and turbulence statistics under oscillatory flow conditions. We use a novel Volumetric Particle Velocimetry technique (3D-PIV) to capture instantaneous and averaged three-dimensional (3D), three-component (3C) velocity fields. Thus, we provide three-dimensional flow organization, turbulence, and coherent structures produced by vegetation as a function of its 3D morphology. This study improves our understanding on aquatic vegetation—flow interaction in habitats exposed to oscillatory flows and its implication on ecosystem altering processes such as enhanced mixing and sediment transport.

## 2 Materials and methodology

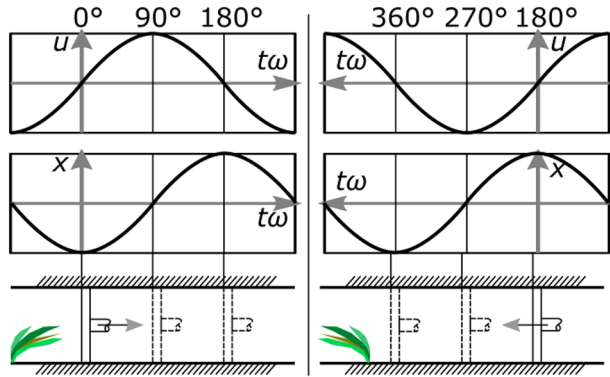
### 2.1 Experimental setup

Figure 1 shows an illustration of the experimental setup. A U-shaped oscillatory tunnel, 0.203 m-wide, 0.254 m-high, and 4.0 m-long, with a 1.52 m-long testing section, is used to impose sinusoidal cross-sectional uniform flows over a single plant. It is provided with a piston-actuator system controlled through a LabView script that allows a maximum stroke of 0.10m and minimum oscillation period of 3.0 s. The tunnel has smooth transparent acrylic walls, allowing for studies on boundary layer and coherent structures; e.g., [38, 39].



**Fig. 1** Experimental setup: oscillatory 203 × 254 mm-cross section tunnel and 3D PIV system

**Fig. 2** Sinusoidal motion of the piston, longitudinal velocity  $u$ , and its relative position to the plant as piston moves away from (0–180) and towards the plant (180–360)



**Table 1** Summary of flow conditions as a combination of oscillation amplitude  $A$  and period  $T$ . Maximum volumetric averaged velocity  $U_\infty$  and  $Re$  for the non-vegetated cases are shown (See Sect. 3.2 for details)

Flow	Nominal piston stroke (mm)	$A$ (mm)	$T$ (s)	Sampling freq. (Hz)	$U_\infty$ (mm/s)	$Re$
A	100	54	3.2	5	99.0	$5.26 \times 10^3$
B	100	54	5.0	3.2	66.0	$3.65 \times 10^3$
C	100	54	10.0	1.6	37.0	$2.30 \times 10^3$
D	50	25	5.0	3.2	32.5	$8.88 \times 10^2$
E	25	14	2.5	6.4	37.7	$5.95 \times 10^2$
F	25	14	5.0	3.2	15.6	$2.05 \times 10^2$

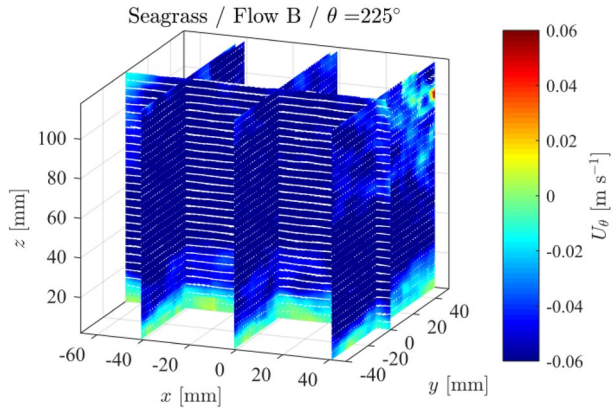
Figure 2 represents the piston position and corresponding velocity with respect to the plant, as it moves away from (0°–180°) and towards the plant (180°–360°).

3D-PIV measurements are taken with a TSI V3V system (TSI, Inc). It uses a coplanar array of 3 PowerView, 4MP (2048 × 2048), 180 fps cameras, and an Nd:YAG, 100 mJ, 532 nm, 100 Hz, dual cavity PIV laser to measure instantaneous 3D, 3C velocity fields at a fixed  $12 \times 12 \times 10 \text{ cm}^3$  space, at a maximum sampling frequency of 100 Hz, with a 2 mm-spatial resolution. A detailed description of the technique can be found in Pothos et al. [51]. This novel technique has been used in ecohydraulic investigations of swimming mechanisms; e.g., [11, 26, 28], but not yet in vegetated flows. Six flow conditions are assessed as a combination of three stroke amplitudes,  $A$ , and four periods,  $T$ , as indicated in Table 1. Sampling rate for the V3V system is selected such that 16 instantaneous velocity fields are measured within one wave period. Single and flexible plants are placed at the centerline of the tunnel ( $y = 0 \text{ mm}$ ) and at 197 mm in the  $x$ -direction away from the center of the measuring volume ( $x = 0 \text{ mm}$ ). It guarantees that the deflected stems of the plants will not interfere with the laser illumination of the measuring volume.

Figure 3 shows an example of the available data, with the phase averaged longitudinal velocity,  $U_\theta$ , at a given phase ( $\theta = 225^\circ$ ), for flow condition A in the presence of a single seagrass-type plant. While only four planes are shown to ease visualization, the system provides the same spatial and temporal resolution for any horizontal and vertical plane within the sampling volume. Such a capability becomes important for irregular plant morphologies (as is the case for the present study), and randomly distributed vegetation arrays



**Fig. 3** Phase-averaged longitudinal velocity field,  $U_\theta$ , for a single seagrass under flow condition A. Oscillation period and stroke amplitude are 3.2 s and 54 mm, respectively. Colormap indicates magnitude of  $U_\theta$ , with arrows for mean velocity vectors in the visualized planes



(the focus of a future study), where flow structure and thus mixing and sediment transport patterns depend on spatial arrangement and geometry of the vegetation.

### 2.2 Synthetic vegetation

Three plant morphologies are evaluated: (a) 'seagrass', characterized by flat, elongated, blade-shaped leaves; (b) 'leafy', characterized by ascending stems with rounded and flat leaves running along each stem; and (c) 'spikey', showing needle-like leaves, arranged in crown-shaped foliage (Figs. 4, 5). Plastic surrogates are used to represent these morphologies, made of the same plastic material but distinct shapes. Material density  $\rho$  is  $840 \text{ kg m}^{-3}$  and Young's modulus  $E$  is  $5.33 \times 10^7 \text{ Pa}$ . These two intrinsic properties of the material are true for each morphological element of the plant (stems, leaves, branches). These values agree with biomechanical properties of aquatic vegetation

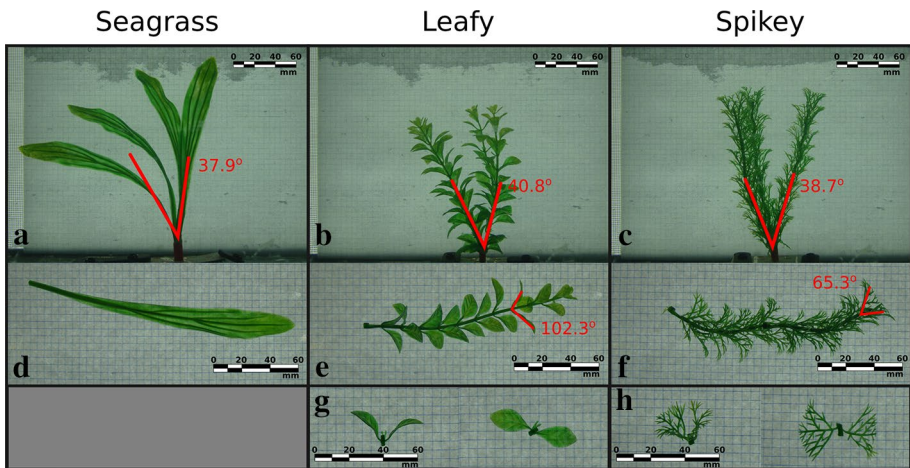


**Fig. 4** Synthetic plants representing: **a** 'seagrass', **b** 'leafy', and **c** 'spikey' morphologies, their respective stem morphology (**d–f**) and their leaf morphology (**g–h**)

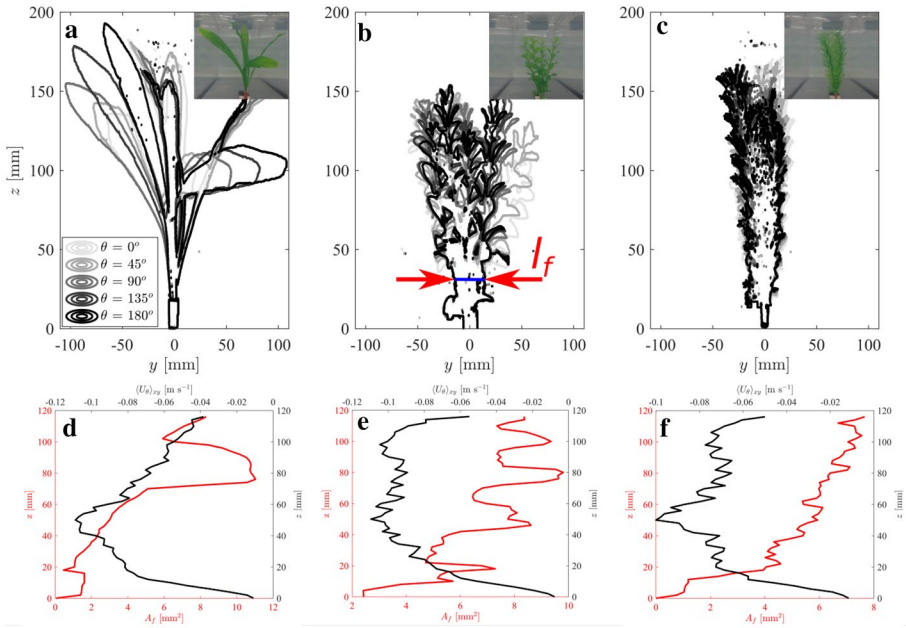


**Fig. 5** Synthetic plants representing: **a** 'seagrass', **b** 'leafy', and **c** 'spikey' morphologies. They show frontal area contours variation under flow condition A. Top insets show raw images from submersed camera. Lower plots **d–f** present an example of frontal area variation under flow condition A

( $\rho = 664.17\text{--}1032.34 \text{ kg m}^{-3}$  [66] and  $E = 5.56 \times 10^6\text{--}1.99 \times 10^8 \text{ Pa}$  [48]) and fall within the range of values used in previous studies to replicate aquatic vegetation-flow interaction ( $\rho = 670\text{--}920 \text{ kg m}^{-3}$  and  $E = 5.0 \times 10^5\text{--}2.4 \times 10^9 \text{ Pa}$ ) e.g., [2, 13, 32]. Flexural strength is defined as the product between Youngs modulus  $E$  and the second moment of the cross-sectional area  $I$  perpendicular to the force [4]. Table 2 summarizes flexural strength of the tested models considering cross-sectional geometry of their stems.

Seagrass plant is formed by 5 leaves, 195 mm-long, 1.72 mm-thick, and 21.5 mm-wide. Leafy plant consists of 4 ascending branches 144 mm-long with approximately 23 leaves 1.72 mm-thick and 13.5 mm-wide. Spikey plant is formed by 3 branches 164 mm-long with 22 crown-shaped arrays of spikes. Spikey shoots are fan-shaped leaves with 1.02 mm-diameter spikes that branch out from large into smaller spikes; with their lengths ranging from 23.3 to 2.7 mm. Species like like *Zostera* subgenus *Zosterella*, *Thalassia*, and *Posidonia* fall under Seagrass type of morphology [25]. Leafy morphology includes species with environmental interest such as *Micranthemum umbrosum* sp., *Elodea candensis*, *Hyrophila polysperma*, and *Cedamine lyrata*. *Cabomba aquatica*,

**Table 2** Flexural strength of plant models measured as the product of Youngs modules  $E$  and second moment of cross-sectional area of the stem  $I$

Plant model	$EI$ (N m <sup>2</sup> )
Seagrass	$5.9 \times 10^{-5}$
Leafy	$7.6 \times 10^{-5}$
Spikey	$3.7 \times 10^{-4}$

*Cabomba coraliniana*, *Ceratophyllum echinatum* A. Gray, and *Limnophila indica* are just a few examples of Spikey morphology.

Frontal area is calculated from videos taken with a submerged camera (GoPro Hero4-Black) downstream of each plant at 30 fps (30 Hz) under each flow condition prior to velocity measurements. 8.3 MP-frames from video recordings are extracted at the sampling frequency shown in Table 1. Since fps from the camera is significantly higher than sampling frequencies, we are able to match precisely the velocity measurements with the pictures of vegetation frontal area. Figure 5 illustrates the frontal contour variation of these morphologies from 0° to 180°. The top insets show a raw image from the downstream camera, and bottom insets show an example of the frontal area profile for one of the flow conditions investigated, to be discussed in next section.

### 2.3 Method of analysis

Longitudinal, lateral, and vertical coordinates are defined as  $x$ ,  $y$ , and  $z$  axis, respectively; with their corresponding velocity components  $u$ ,  $v$ , and  $w$ . Instantaneous velocity is decomposed according to Eq. 1; where  $u$  is instantaneous velocity,  $U_c$  is time-averaged velocity,  $U_\theta$  is phase-averaged velocity, and  $u'$  is the turbulent fluctuation [43, 64]. Phase-averaged velocity is computed following Eq. 2, where  $N$  is the total number of measured oscillations and  $\omega$  is angular velocity [21, 23].

$$u = U_c + U_\theta + u' \tag{1}$$

$$U_\theta = \frac{1}{N} \sum_{n=1}^N [u(x, y, z, \omega(t + nT)) - U_c] \tag{2}$$

Spatial-averaging is denoted by angle brackets  $\langle \rangle$ . Equations 3a, 3b and 3c presents examples of the averaging schemes of  $u$  to average over  $y$  to obtain a single vertical  $xz$  plane (3a), average over  $x$  and  $y$  to obtain a single vertical profile (3b), and average over  $x$ ,  $y$ , and  $z$  to obtain a volumetric average, i.e., a single bulk value representative of the flow conditions. Notice that subscripts indicate coordinates over which averaging took place.  $N_x$ ,  $N_y$ , and  $N_z$  are total points along coordinates  $x$ ,  $y$ , and  $z$ , respectively. Same scheme applies for all other possible vertical and horizontal planes and profiles within the sampling volume (see Fig. 3).

$$\langle u \rangle_y = \frac{1}{N_y} \sum_{j=1}^{N_y} u(x_i, y_j, z_k, \omega t) \tag{3a}$$

$$\langle u \rangle_{xy} = \frac{1}{N_x N_y} \sum_{i=1}^{N_x} \sum_{j=1}^{N_y} u(x_i, y_j, z_k, \omega t) \tag{3b}$$

$$\langle u \rangle_{xyz} = \frac{1}{N_x N_y N_z} \sum_{i=1}^{N_x} \sum_{j=1}^{N_y} \sum_{k=1}^{N_z} u(x_i, y_j, z_k, \omega t); \tag{3c}$$

Phase-averaged turbulence kinetic energy ( $TKE_\theta$ ) is computed according to Eq. 4 [50].

$$TKE_{\theta} = \frac{1}{2} \sqrt{(u'^2)_{\theta} + (v'^2)_{\theta} + (w'^2)_{\theta}} \tag{4}$$

### 3 Results and discussion

#### 3.1 Vegetation frontal area

Figures 6 and 7 present the vertical variation of phase-averaged frontal area at  $\theta = 0^{\circ}, 90^{\circ}$ , and  $270^{\circ}$  for the three plant types. We explore the effect of changing period while keeping a constant oscillation excursion ( $A = 54 \text{ mm}$  with  $T$  varying from 3.2 to 10 s in Fig. 6), and

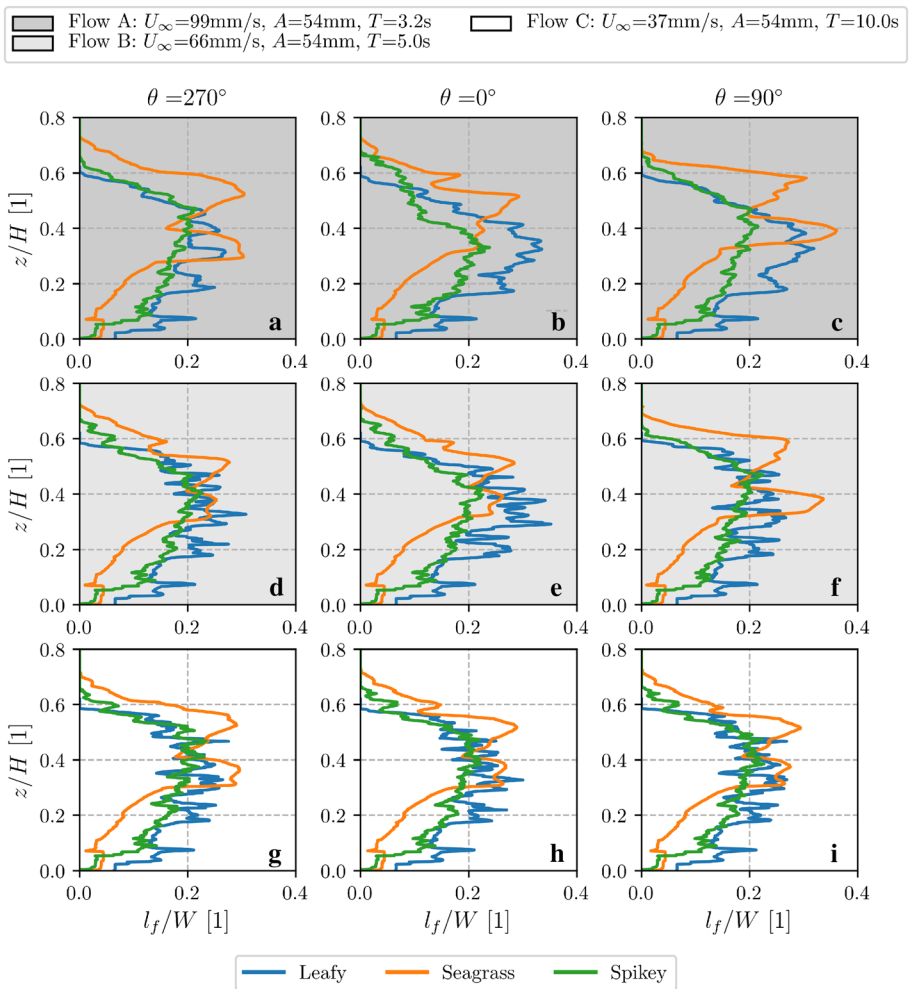


**Fig. 6** Vertical profile of normalized phase-averaged frontal obstructed area at three phases,  $\theta = 0^{\circ}, 90^{\circ}$ , and  $270^{\circ}$ . Blue line: leafy, orange line: seagrass, green line: spikey. Depth is normalized by tunnel height  $H$ , frontal area normalized by tunnel width  $W$ . Cases with constant  $A = 54 \text{ mm}$  are shown

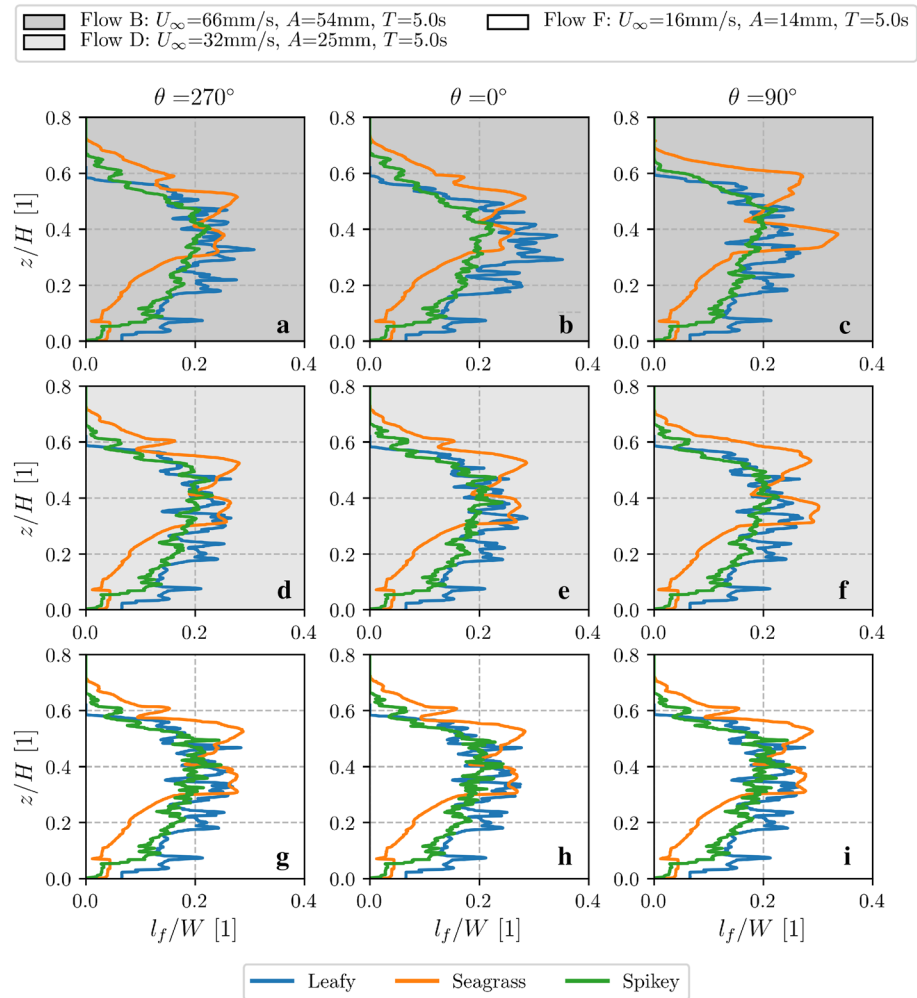


**Fig. 7** Vertical profile of normalized phase-averaged frontal obstructed area at three phases,  $\theta = 0^\circ, 90^\circ,$  and  $270^\circ$ . Blue line: leafy, orange line: seagrass, green line: spikey. Depth is normalized by tunnel height  $H$ , frontal area normalized by tunnel width  $W$ . Cases with constant  $T = 5$  s are shown

the effect of varying excursion while keeping a constant period ( $T = 5$  s with  $A$  varying from 54 to 14 mm in Fig. 7). Normalized frontal area is calculated as the fraction of tunnel width obstructed by the plant,  $l_f/W$ ; where  $l_f(z)$  is cumulative length of actual tunnel width obstructed by a plant at elevation  $z$  (see Fig. 5 for reference).

Spikey and leafy cases show similarities in their frontal area distribution, while seagrass is significantly different. Frontal area profiles of spikey and leafy cases show small-scale variations (a zig-zag pattern) and are more uniformly distributed along the height of the plant, as the clumps and crowns (Fig. 5) are more uniformly distributed along the plant length. Seagrass frontal area profiles are smoother due to the blade-shape of their leaves, and present two peaks due to different leaves positioned at different heights. Frontal area profiles respond more dynamically to shorter oscillation periods, but they are less sensitive

to variations on oscillation excursion. In flow C (Fig. 6g–i), frontal area profiles do not show any evident change over a deceleration-acceleration cycle; whereas a more dynamic change is observed under flow condition A (Fig. 6a–c). Since rearrangement of vegetation canopy is associated with passive and active interactions to reduce drag [5], the observed plant alignment is a relevant parameter to predict the impact of vegetation on flow.

## 3.2 Flow structure: spatial organization

### 3.2.1 Velocity

Table 1 shows a summary of maximum velocity  $U_\infty$  and Reynolds number ( $Re = U_\infty A/\nu$ ) for non-vegetated cases.  $U_\infty$  corresponds to the maximum absolute value of the longitudinal, volumetric-, phase-averaged velocity (see Eq. 5).

$$U_\infty = \max \left( \left| \langle U_\theta \rangle_{xyz} \right| \right) \quad (5)$$

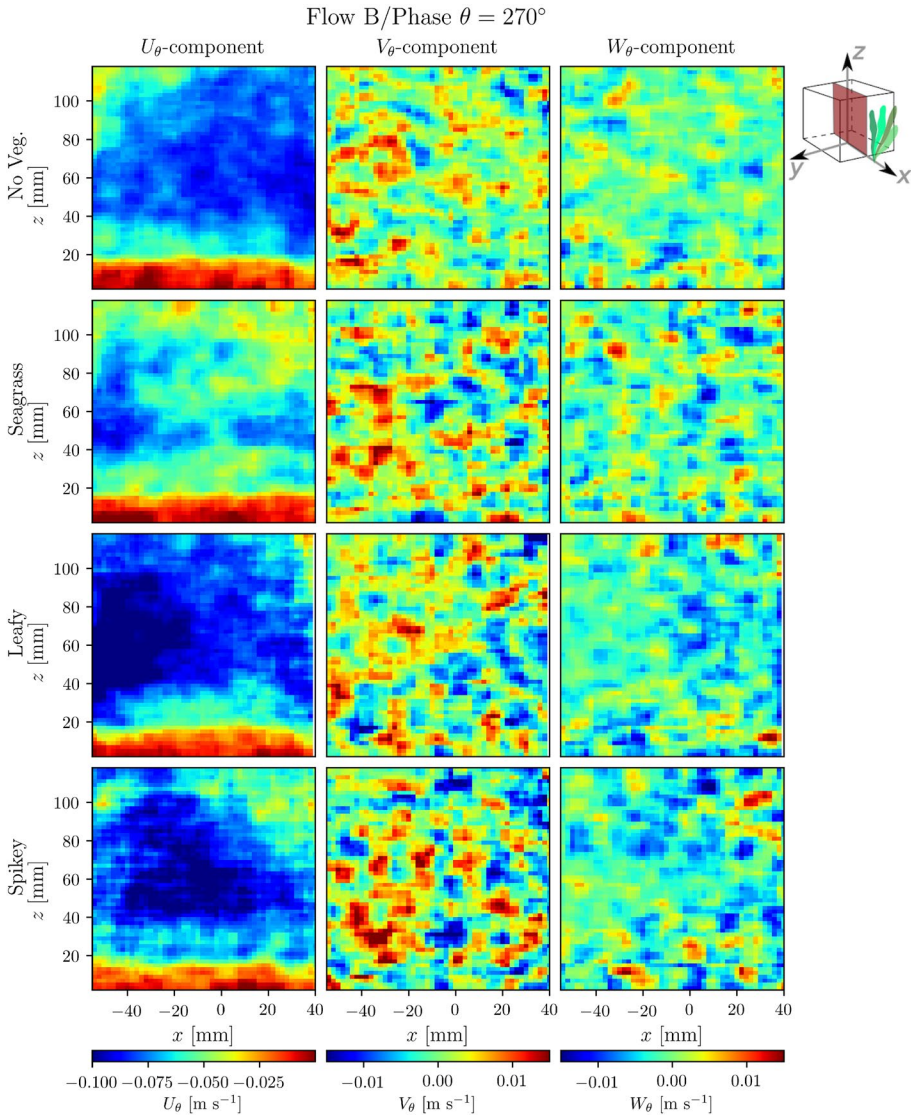
A time average of the longitudinal velocity over several periods shows a non-zero underlying current  $U_c$ . This velocity is attributed to remaining momentum after the piston changes direction.

Figure 8 shows velocity fields over the vertical  $x$ – $z$  plane at the centerline of the tunnel ( $y = 0$  mm), for case B ( $T = 5$  s,  $A = 54$  mm) for all three plants. Flow is predominantly aligned in the  $x$ -direction and negative as phase  $\theta = 270^\circ$  corresponds to the negative-velocity peak. Longitudinal velocity is consistently uniform in the  $x$ -direction. A clear boundary layer is noticed with low near-bed velocities growing until reaching outer flow speeds above  $z = 20$  mm. Velocity vectors are clearly aligned in the longitudinal direction for the non-vegetated case, but they show clear variations as flow moves past the plant, with larger vertical component clearly noticed around  $z = 100$  mm at the regions closest to the plant.

As a single plant, there is a low impact on the average longitudinal velocity field (as is the case with very sparse canopies), but the interactions of the oscillatory flow with the moving plant clearly alter the 3D structure of the flow, as noticed by the larger lateral velocities identified in Fig. 8 past the plants. The different plant morphologies force fluid parcels to move laterally generating shedding vortices at multiple scales. Keulegan–Carpenter number ( $KC = U_\infty T/L$ , where  $L$  is the stem-shoot width) ranges from 11 to 19 for these morphologies; which results in additional asymmetric shedding vortices according to Guilmineau and Queutey [15]. Apparent size of these eddies varies as a function of plant geometry. Areas of organized flow scale with leaf size and crown-shaped leaves of leafy and spikey morphologies, respectively (20 mm and 10 mm). For seagrass with blade-shape, long, and flexible leaves, a smaller effect on lateral velocity is expected under uniform flow conditions [5], but bending of the plant under oscillatory conditions creates a clear 3D flow. Such heterogeneity of lateral velocity can enhance lateral dispersion, both as a function of vegetation density [58] and as a function of plant morphology.

Figures 9 and 10 present phase-averaged velocity fields in horizontal  $x$ – $y$  planes at  $z = 2$  mm (near the bottom, Fig. 9), and at  $z = 100$  mm (Fig. 10) as the piston accelerates towards the plant ( $\theta = 225^\circ$ ). Horizontal in-plane velocity vectors and magnitudes of vertical velocities represented by the colormap near the bed (Fig. 9) show areas of large negative and positive vertical velocity, coupled with local perturbations of  $U_\theta$  and  $V_\theta$ , which are more prevalent and with higher intensities in vegetated cases.

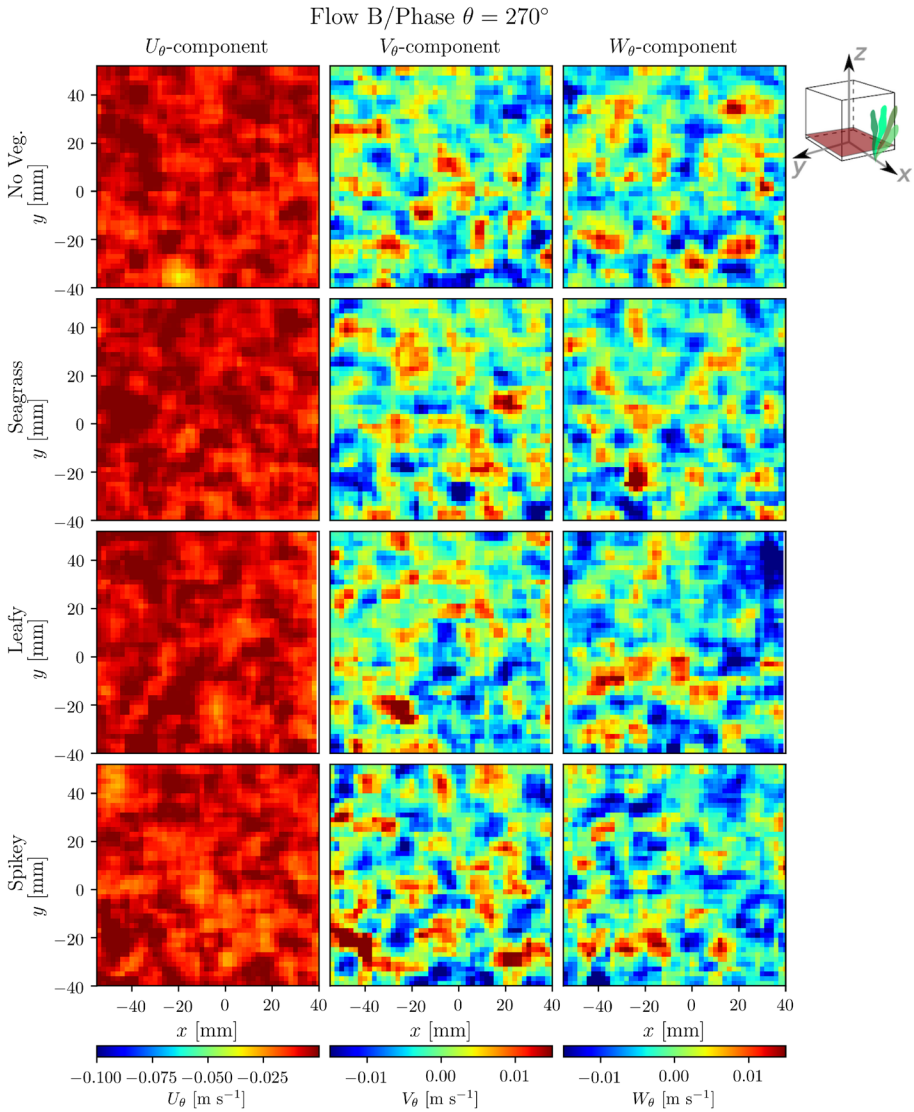




**Fig. 8** Phase-averaged velocity field at vertical  $x$ - $z$  plane at  $y = 0$  mm under flow condition B,  $T = 5$  s and  $A = 54$  mm

Longitudinal velocities are smaller at this near-bed location (see Fig. 8), such that the vertical and lateral component can be more significant to determine bed effects (total stress and effect on sediment transport). In accelerating phases, low-velocity fluid parcels are moved upward from the bottom (ejections) and high-velocity fluid parcels are transported downward from higher elevations (sweeps) [21, 23, 64]. The bed thus becomes subject to vortices set by the plant morphology as they are swept towards the bed. The detected flow spatial organization can influence patterns of near-bottom sediment transport and bedform development.

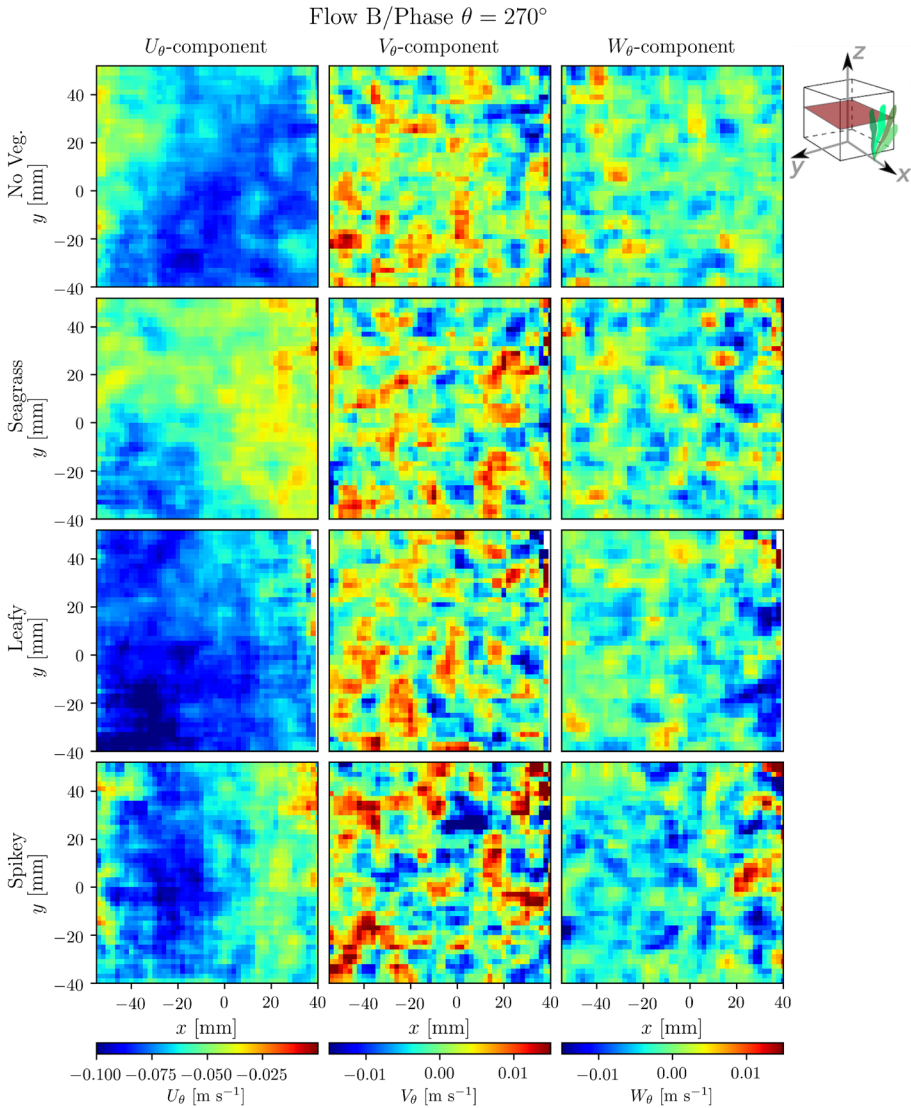




**Fig. 9** Phase-averaged velocity field at a horizontal  $x - y$  plane at  $z = 2$  mm under flow condition B,  $T = 5$  s and  $A = 54$  mm

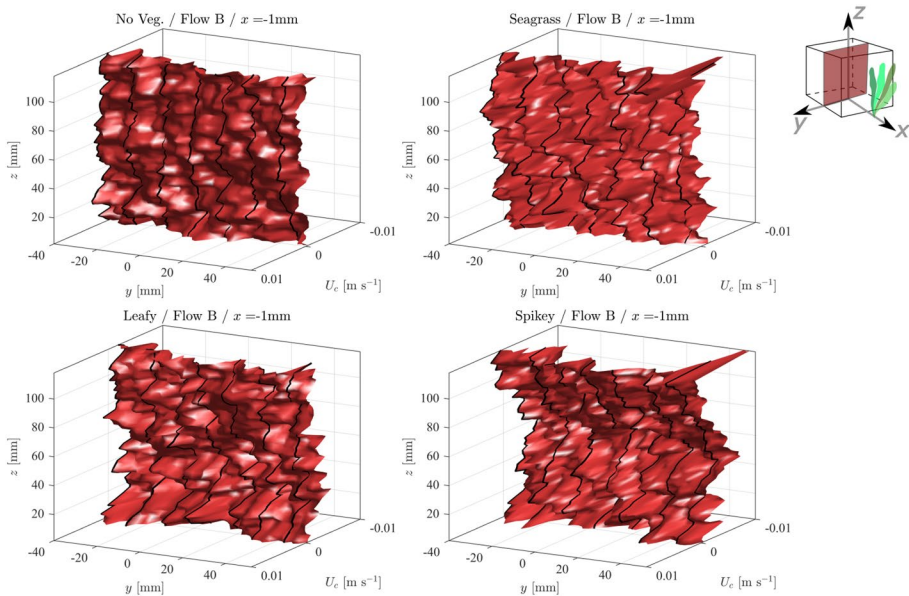
In Fig. 10, the longitudinal velocity component is prevalent. However, large average fluctuations are noticed in the proximity of plant locations, with a more noticeable velocity divergence for seagrass and spikey plants. While stiffness is not a controlled parameter in this experiment; the morphology and freedom to deform to align with the flow induces anisotropic flow organizations at a different degree for each plant type.

Figure 11 shows longitudinal velocity, time averaged over several periods, on a vertical  $y - z$  plane, perpendicular to wave propagation, at a location  $x = -1$  mm, to identify patterns in the underlying current  $U_c$ . Underlying current is defined here as the resulting



**Fig. 10** Phase-averaged velocity field at a horizontal  $x$ - $y$  plane at  $z = 100$  mm under flow condition B,  $T = 5$  s and  $A = 54$  mm

flow after time-averaging the velocity fields over a certain number of oscillation periods. While this non-zero value can be driven by small asymmetries in the piston motion driving the flow, the structure and patterns noticed in Fig. 11 highlight the differences created by the obstructions, and are akin to effects observed in other oscillatory tunnels and wave flumes. See for example; Tinoco and Coco [61], and Luhar and Nepf [32]. Further volumetric-averaging of  $U_c$  shows that the net longitudinal velocity is practically negligible ( $O(10^{-3} \text{ m s}^{-1})$ ), thus ensuring continuity is being satisfied.  $U_c$  varies around  $\pm 0.01 \text{ m s}^{-1}$ , with strong fluctuations in the presence of vegetation. In the no vegetation



**Fig. 11** Longitudinal velocity distribution of underlying flow at  $x = -1$  mm. Oscillation period and stroke amplitude are 5 s and 54 mm, respectively. Black lines over the surface correspond to longitudinal velocity profiles

case, it contributes to approximately 8 % of the maximum outer velocity  $U_\infty$  and causes  $A$  to become larger than half of the piston stroke by a similar proportion (see Table 1). Positive and negative peaks of longitudinal velocity increase progressively in seagrass, leafy, and spikey morphologies. Velocity field also shows some concavity along the centerline of the tunnel ( $y \approx 0$  mm) for leafy and spikey plants, a behavior associated with lateral and vertical wakes behind the plants.

To better understand the changes in velocity for different plant species, we look at how the plants bend with the flow, using side-view recordings and identifying their maximum excursions on both directions for all flow conditions (Fig. 12), as they experience displacement in the positive  $x$ -direction (between  $0^\circ$ – $180^\circ$ ), and in the negative  $x$ -direction (between  $180^\circ$  and  $360^\circ$ ). Lateral displacements range from 4.9 to 105.1 mm. It is noticed that: (a) Not all stems and blades experience the same range of motion, specially noticed for the seagrass case, where the one blade bent the most towards the negative  $x$ -direction barely moved throughout the full oscillation (noticed by the overlap between shaded profiles), while other blades (seagrass) and stems (spikey and leafy) rotate almost  $90^\circ$  in an  $x$ – $z$  plane during one period (cases A and B, Fig. 12); and (b) Looking closely at both Figures 5 and 12 we notice spikey and leafy plants sway mostly around the  $y$ -axis within vertical  $x$ – $z$  planes, while seagrass experiences more significant rotation around the  $z$ -axis, with blades changing orientation with respect to the flow at different phases, in contrast with expected streamlining under unidirectional conditions.

These two observations show that a static plant morphology can inform us of the scale of the expected eddies, but a dynamic analysis and bending observations are critical to identify their orientation and location. As plants reach their maximum excursion towards either the negative or positive  $x$ -direction, they get closer to the bed, potentially increasing their effect on near-bed velocities, shear stress, and thus their effect on sediment transport.

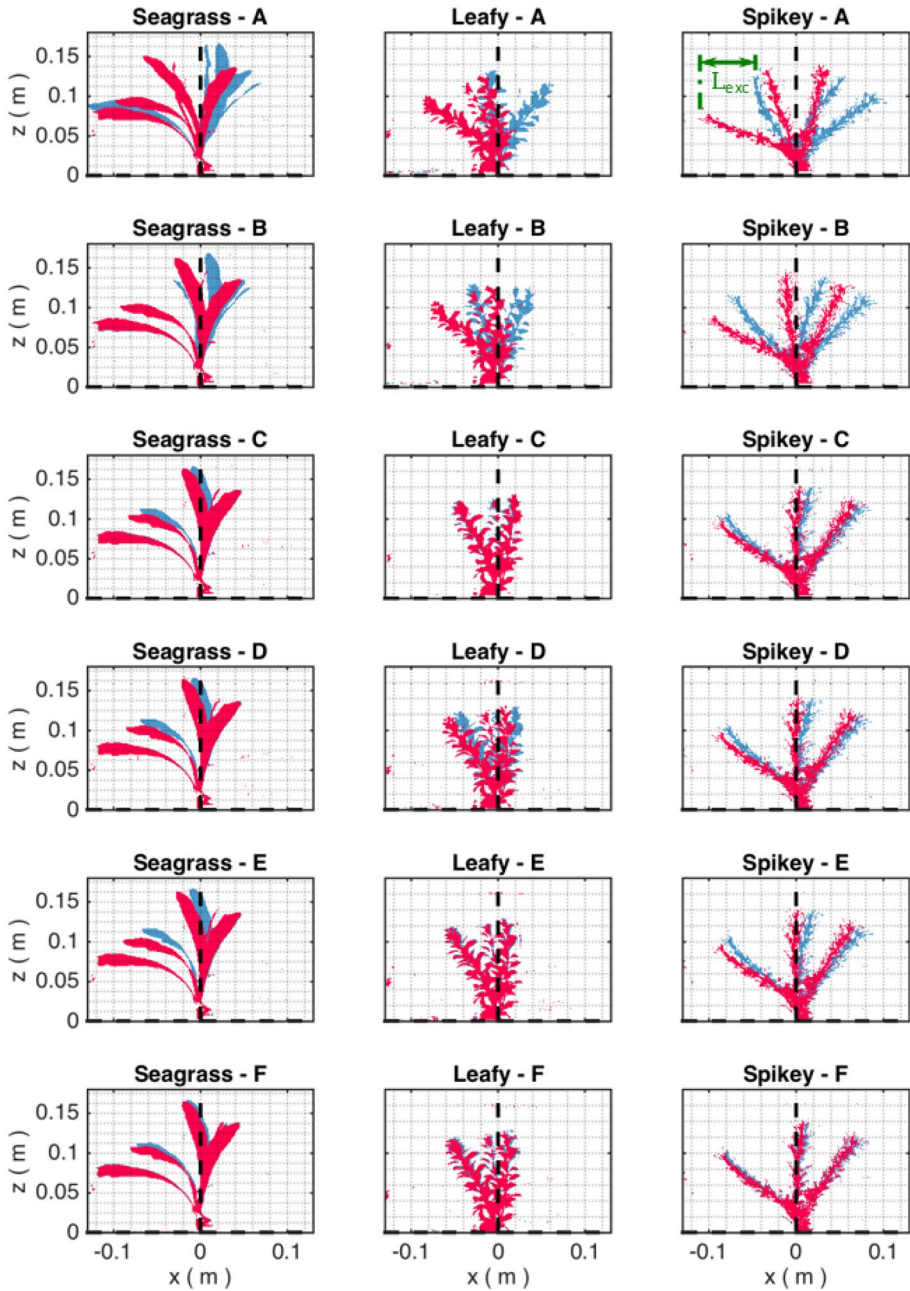


**Fig. 12** Lateral displacement range for the three species at all flow conditions. Positive  $x$  displacement (blue) between 0 and 180. Negative  $x$  displacement (red) between 180 and 360. Excursion length,  $L_{exc}$ , is represented in top-right subplot

Figure 12 shows that plant excursions are mostly dependent on maximum speed (see Table 1) rather than  $A$  or  $T$  alone. Keeping the same  $A = 54$  mm while changing  $T = 3.2$  s (A), 5.0 s (B), and 10.0 s (C), results in a decrease in maximum velocity from 99 to 37 mm/s, yielding large plant excursions for A and minimum motion for C. Keeping the same  $T = 5$  s while varying  $A = 54$  mm (B), 25 mm (D), and 14 mm (F), results in reduction of maximum velocity from 66 mm/s (B) to 15.6 mm/s (F), and thus barely noticeable motion in F. This pattern is also evident in cases C, D, and E, with chosen combinations of  $T$  and  $A$  that yield similar maximum speeds (32.5–37.7 mm/s) and show almost identical plant excursions.

Drag force ( $F_D$ ) acting on flexible vegetation depends on the relative velocity between flow and plant. This is conceptualized by Zeller et al. [70] using the maximum plant excursion  $L_{exc}$  and oscillation excursion  $A$  ( $KC_{exc} = A/L_{exc}$ , see Fig. 12). Drag coefficient  $C_D$  follows a power-law relationship with Keulegan–Carpenter  $KC_{exc}$  number when wake development scales with  $A$  and obstruction scales with  $L_{exc}$  ( $C_D \propto (A/L_{exc})^{-1.7}$ ) [70]. Cauchy number  $Ca$  measures the ratio between drag and rigidity-restoring forces [33]. This balance indicates how prone flexible vegetation is to streamline or stay upright under certain flow conditions. The relative strength of drag force with respect to plant rigidity (rigidity force  $F_R$ ), expressed in Eq. 6, depends on the maximum velocity by a power of 2; where  $\rho_w$  is water density,  $A_f$  is stem frontal area, and  $l$  is stem length. Therefore, the larger weighted contribution to drag coming from  $U$  with respect to  $A$  makes plant excursion more dependent on maximum velocity than oscillation excursion or period alone. Furthermore, the ratio between oscillation excursion and plant size becomes a limiting factor for flow-vegetation behavior and turbulence production. Luhar and Nepf [32] explain that flow-vegetation interaction resemble steady unidirectional behavior at the limit where  $A$  is larger enough than vegetation length  $l$ . Inertia forces from the plant acting upon the flow may be neglected because the relative velocity between flow and vegetation is similar to the flow velocity itself. Investigating Vogel number effects on velocity skewness, Pan et al. [47] found that more negative Vogel number (associated with increasing  $A/L_{exc}$ ) correlates with peaks in longitudinal and vertical velocity skewness (strong sweeps) that penetrates into near-bed elevations. Such effect can potentially enhance resuspension and favor mass exchange with above-canopy regions.

$$Ca = \frac{F_D}{F_R} = \frac{C_D U_\infty^2 \rho_w A_f l^2}{2 EI} \quad (6)$$

$$B = \frac{F_B}{F_R} = g(\rho_w - \rho_v) V_{stem} \frac{l^2}{EI} \quad (7)$$

Buoyancy parameter,  $B$ , is a dimensionless parameter that measures the relative contribution between buoyancy- and rigidity-restoring forces [2]. It is defined in Eq. 7 as the ratio between buoyancy and rigidity forces ( $F_B/F_R$ ); where  $\rho_v$  is the density of the plants,  $g$  is gravitational acceleration, and  $V_{stem}$  is stem volume. Figure 13 presents the  $Ca$  variation with respect to  $B$  and  $KC_{exc}$ . Drag (and thus  $Ca$ ) increases with maximum flow velocity and buoyancy coefficient  $B$ . Higher buoyancy contributes to keep stems upright longer, resulting in shorter plant excursions (smaller  $KC_{exc}$ ). In contrast, a weaker impact of  $A$  is seen in flow C and E of Fig. 13. While both have the same maximum velocity, drag force is stronger in flow E ( $A = 0.05$  m) than in flow C ( $A = 0.01$  m) by almost an order



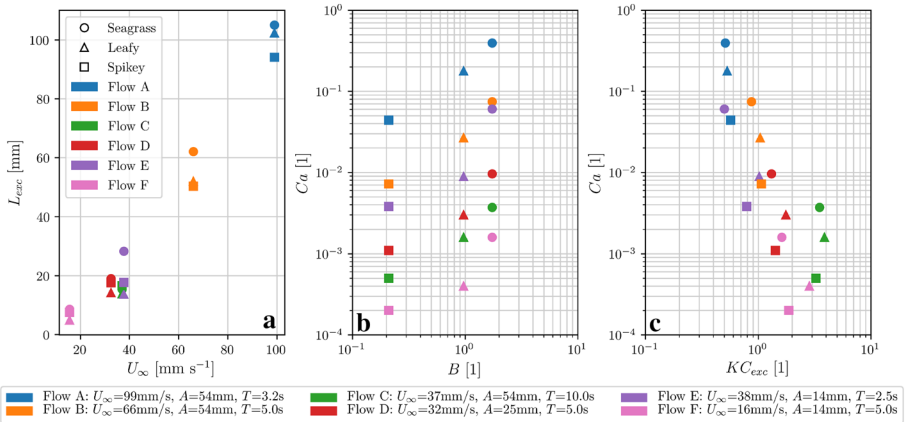


**Fig. 13** Cauchy number,  $Ca$ , as function of buoyancy coefficient,  $B$ , and Keulegan–Carpenter number based on plant excursion,  $KC_{exc}$ , at all flow conditions

of magnitude. Data also show that canopy morphology affects the balance between drag, buoyancy, and rigidity forces. Even though all synthetic plants used in this work are made out of the same material, second moment of inertia  $I$ , stem volume, and frontal area, are necessarily function of vegetation geometry.

### 3.2.2 Velocity defect profiles

The effect of plant morphology is investigated by looking at the normalized velocity defect profiles, calculated from Eq. 8, where “veg” and “no veg” denote vegetated and no vegetated conditions, respectively.

$$\Delta U_{xy}(z, \omega t) = [U_{xy}(z, \omega t)]_{veg} - [U_{xy}(z, \omega t)]_{no\ veg} \tag{8}$$

Results are shown in Figs. 14 and 15. An additional case with a single rigid cylinder, with diameter of 11.3 mm was conducted for comparison at all flow conditions. Profiles of longitudinal phase-averaged velocity show a decrease in the presence of vegetation for the phases presented in Figs. 14 and 15. The effect of vegetation decreases with increasing  $T$  (i.e., when reducing maximum velocities). Velocity defect past the plants becomes more sensitive to  $A$  variation than to  $T$  variation. Differences between longitudinal velocity defect profiles at phases 90° and 270° are attributed to the relative location of the measuring volume with respect to the vegetation and the flow direction. Over negative-velocity phases, the measuring volume is located at the wake zone of the vegetation (see Figs. 1, 2). While, it is found “upstream” of the plants over the positive-velocity phases. Although no consistent  $\Delta \langle U_{\theta} \rangle_{xy}$  pattern based only on plant morphology is found, it is noticed that the profiles of velocity defect for the leafy and spikey cases resemble the general trend of their frontal area profiles, with a zig-zag small-scale fluctuation in both frontal area and velocity profiles. Overall, the spikey case presents a larger effect on longitudinal velocity, almost on par with the rigid cylinder, in particular for the higher velocity cases (A and B).

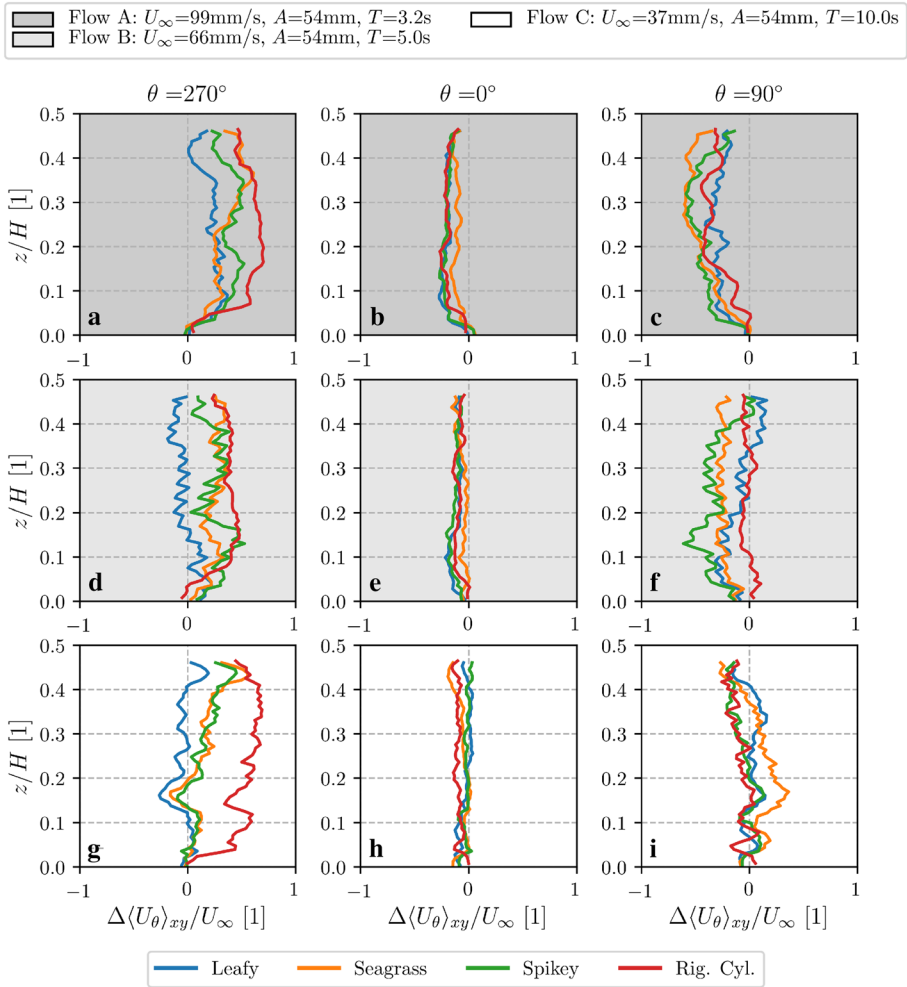


**Fig. 14** Profiles of longitudinal velocity defect. Blue line: leafy, orange line: seagrass, green line: spikey, red line: cylinder. Flow conditions A, B, and C where  $A = 54\text{ mm}$

### 3.2.3 Vorticity

Since the plants generate eddies at multiple scales, and their changing orientation and position (Figs. 5, 12) yields eddies on various planes, we conduct an analysis of vorticity to identify their net effect. Figure 16 presents iso-surfaces of phase-averaged vorticity with respect to the  $y$ -axis,  $\omega_y$ , under flow B at accelerating phase  $\theta = 225^\circ$ . The iso-surfaces are integrated with  $x$ - $z$  planes color maps at  $y = -20\text{ mm}$  and  $y = 20\text{ mm}$ .

The 3D vorticity captures tubular coherent structures described first by [9] and later studied by [38]. Previous lacking of 3D measurements limited experimental identification and description of these structures [38]. Results from the non-vegetated case agree with Mujal et al.'s experiments [38]: tubular coherent structures form at early accelerating phases and are ejected half-way of the accelerating phases; at which point new coherent



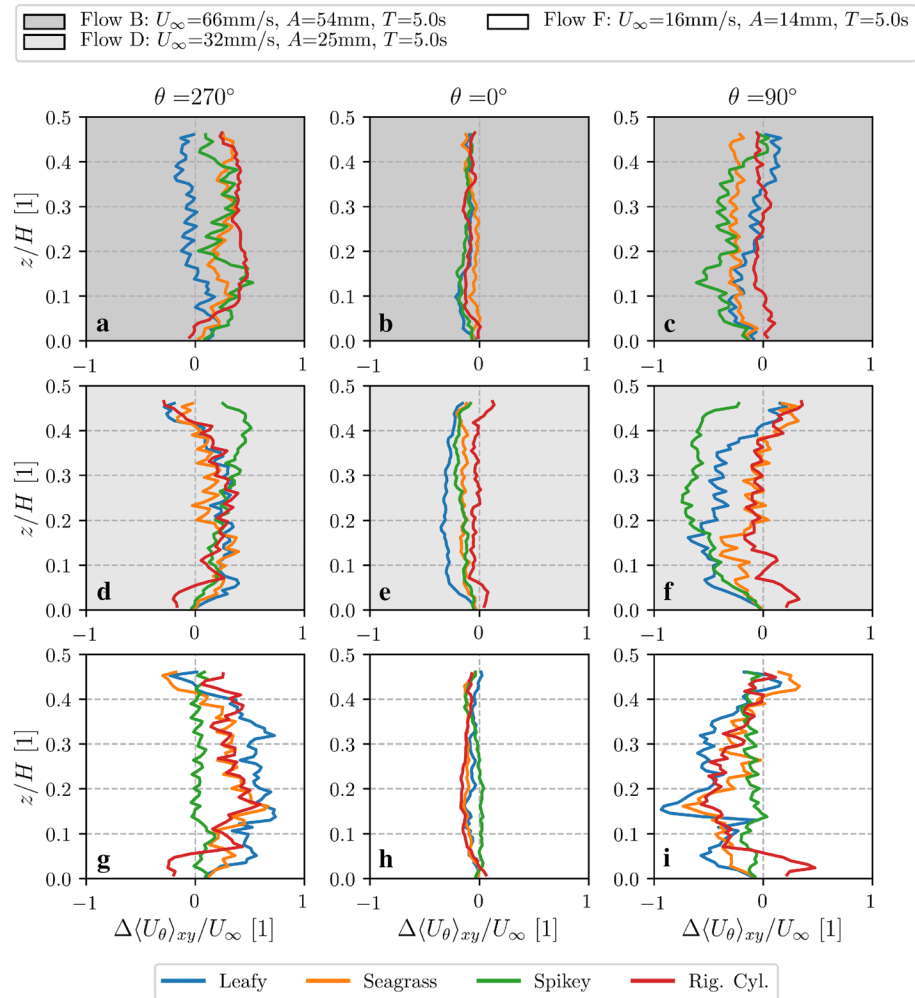


**Fig. 15** Profiles of longitudinal velocity defect. Blue line: leafy, orange line: seagrass, green line: spikey, red line: cylinder. Flow conditions B, D, and F where  $T = 5.0$  s

structures start developing close to the wall (Fig. 16). The non-vegetated case shows this tubular surfaced uniformly aligned near the bed, which contrast with the patterns observed past the three plant types, where production and ejection of elongated vortices prevails. The tubular coherent structures become segmented by the plant morphology (stem, blades, leaves, and/or needles) over the negative-velocity phases. Figure 16 shows a more irregular, highly 3D vorticity field, with smaller length scale structures for the case of spikey and leafy cases, as expected due to the prevalence of crowns and small leaves for such morphologies in comparison with the long, smooth blades of the seagrass type. Such shorter tubular coherent flow structures generated by the plants with a broader distribution within the water column, in contrast with the near-bed long structures creating a nearly 2D scenario from a flat bed, can alter the spatial development of bedforms under oscillatory flows in presence of flexible vegetation. Tubular vortex in oscillatory boundary layer flows cause

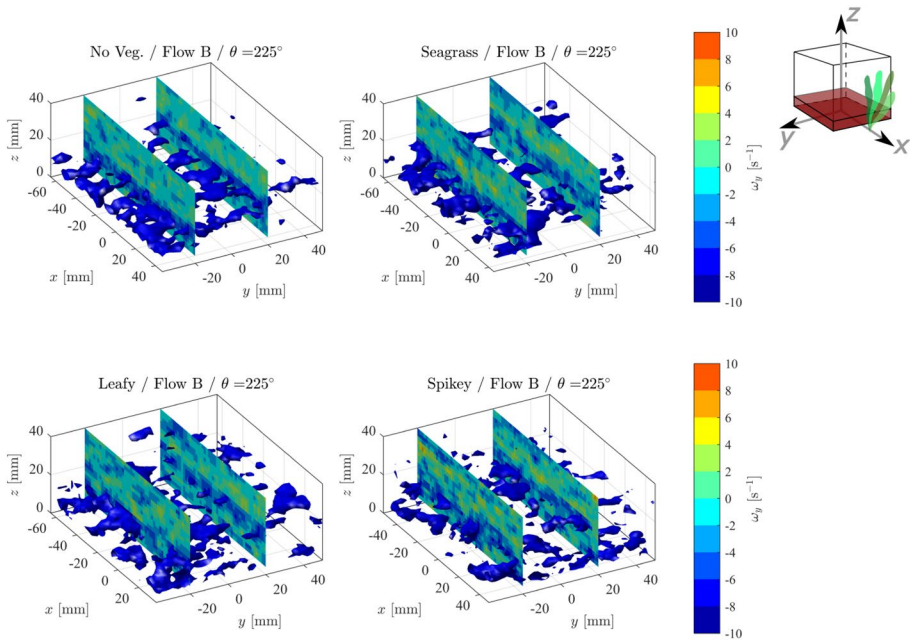


**Fig. 16** Iso-surface of lateral component of vorticity  $\omega_y = 5 \text{ s}^{-1}$  under flow condition B,  $T = 5 \text{ s}$  and  $A = 54 \text{ mm}$ . Two  $x$ - $z$  planes show color maps of  $\omega_y$  at  $y = -20 \text{ mm}$  and  $y = 20 \text{ mm}$

sediment entrainment as they resemble size and strength of vortex shedding over wave ripples [18].

### 3.2.4 Shear stress

Figure 17 presents variation of phase-averaged bed shear stress as a function of phase  $\theta$  and lateral coordinates  $y$  for all three plants, for the maximum and minimum orbital velocities: case A ( $U_\infty = 99.0 \text{ mm/s}$ ), B ( $U_\infty = 66 \text{ mm/s}$ ), and F ( $U_\infty = 15.6 \text{ mm/s}$ ). Since log-law velocity conditions do not fully develop over a complete oscillation [21], spatial distribution of  $\tau_b$  is estimated by the momentum deficit between the outer and the boundary layer velocity [39] (Eq. 9). Bed shear stress corresponds to the estimated shear at our closest measurement to the bottom ( $z = 2 \text{ mm}$ ). It is later normalized by  $\rho U_\infty^2$  from each case. Figure 17 shows the estimated bed shear stress along the  $y$ -axis at  $z = 2 \text{ mm}$  and  $x = 40 \text{ mm}$  for each phase.

$$\frac{\tau(\theta, z)}{\rho} = \int_z^\infty \frac{\partial [U_\infty(\theta) - U_\theta(\theta, z)]}{\partial t} dz \tag{9}$$

The highest phase-averaged shear stress occurs near  $160^\circ$  and  $337.5^\circ$ , following a approximate  $65^\circ$ -phase lag behind the top speeds at  $90^\circ$  and  $270^\circ$ . Hansen and Reidenbach [16] found that bed shear stress is significantly reduced in the presence of patches of vegetation. Yang et al. [68] developed a predictor for bead shear stress in arrays of rigid vegetation

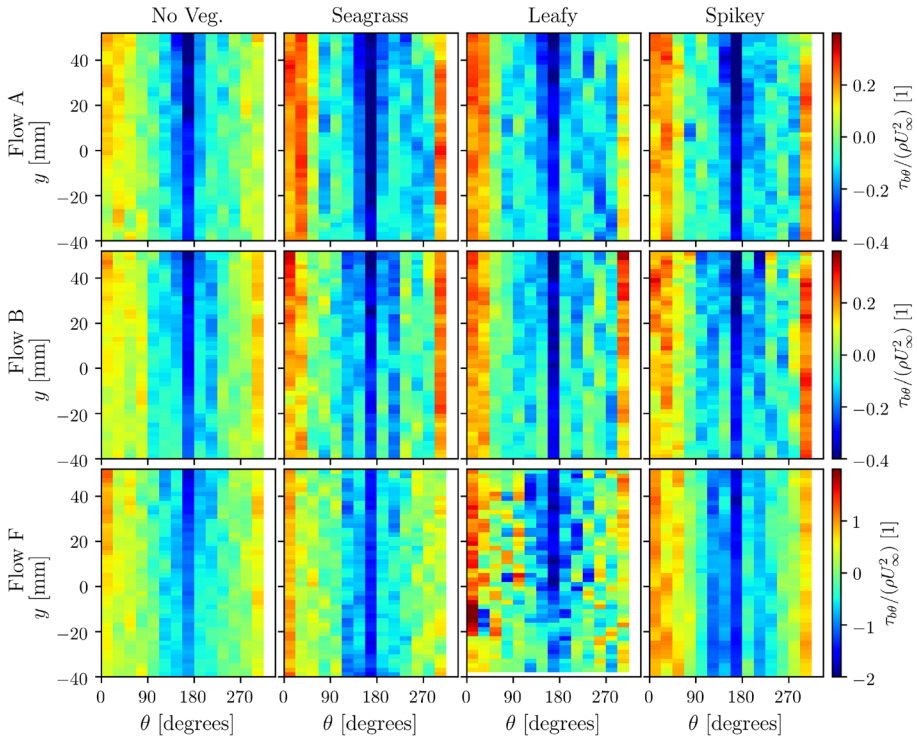


**Fig. 17** Transverse spatial distribution of phase-averaged bed shear stress,  $\tau_{p\theta}/(\rho U_{\infty})$  (1), past the plant, for flow conditions A ( $A = 54$  mm,  $T = 3.2$  s,  $U_{\infty} = 99.0$  mm s<sup>-1</sup>), B ( $A = 54$  mm,  $T = 5.0$  s,  $U_{\infty} = 66.0$  mm s<sup>-1</sup>), and F ( $A = 14$  mm,  $T = 5.0$  s,  $U_{\infty} = 15.6$  mm s<sup>-1</sup>), for all plants studied

using an effective friction velocity that depends on the dampened velocity within the array and either a drag coefficient for the bare bed or the individual plant diameter. As we focus on a single vegetation element, these type of predictors do not directly apply, as we look at how the bending and orientation of the plants can affect stresses locally, and there is not an array dense enough to dampen velocities as in [16, 68]. From Fig. 12 for all cases, and Fig. 5 for case A, we notice the displacement of the three plants under flows A, B, and F. From 180° to 360° the plant bends in the direction of wave propagation (negative  $x$ ), with stems and blades getting closer to the bed toward the measured volume. From 0° to 180°, the blades move towards the positive  $x$  direction, away of the measured volume. The closer proximity of blades and stems to the bed around 270° coupled with the lateral movement of the blades can result in asymmetric effects on the stress distribution. Lateral variations of bed stress with respect to the non-vegetated case are more evident for seagrass and leafy types, consistent with the wider range of motion in the  $y$ -direction, as seen in Fig. 5, whereas the spikey case, which motion is more constrained to the  $x$ - $z$  plane, shows a more uniformly distributed stress in the transverse,  $y$ -direction.

Figure 17 provides a clear picture of the distributed stresses and effect of a single plant due to stems and bed orientation (Fig. 5) and proximity to the bed (Fig. 12), but does not show the changes in magnitude of these stresses. Taking transects from plots in Fig. 17 at  $y = -20$  mm,  $y = 0$  mm, and  $y = 20$  mm along the full cycle, Fig. 18 shows the

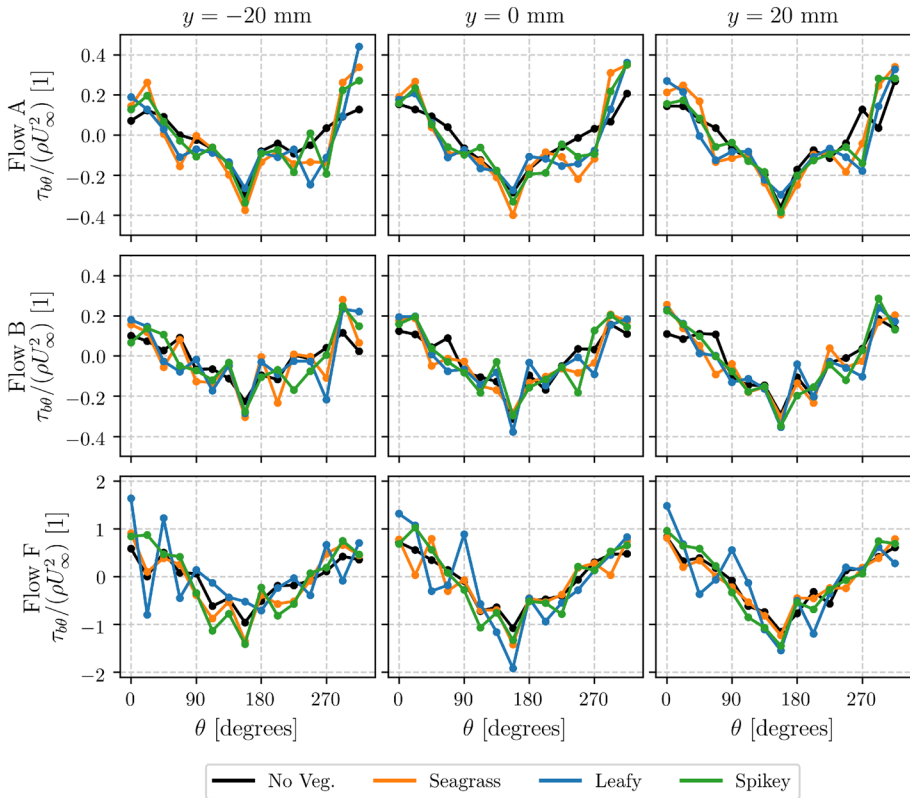


**Fig. 18** Phase-averaged bed shear stress as function of phase along  $y = -20$  mm,  $y = 0$  mm, and  $y = 20$  mm for the three plants investigated, for flow conditions A, B, and F

phase-averaged bed shear stress evolution, as a function of phase, at these three transverse locations. Figure 18 shows more clearly the decrease in mean bed shear stress in the vegetated cases, as well as the asymmetry between  $y = -20$  mm and  $y = +20$  mm data seen in Fig. 17

Plant morphology effect on bed shear stress heterogeneity is stronger in flows with low velocity. Higher variability in bed shear stress is found in flow F, where all plants had very limited range of motions. The degree of velocity alteration becomes more sensitive to plant morphology in low-velocity flows as they are easily disrupted by the vegetation. Leafy case has the greatest impact on bed shear stress distribution compared to the non-vegetated cases. This plant morphology has the shortest plant excursion in flow F and intermediate buoyancy coefficient  $B$  among the three morphologies. Thus, bed shear stress heterogeneity comes from flow separation that take place from a nearly steady standing plant rather than a swaying one.

The impact on bed shear stress variability as a function phase is higher in vortex shedding from a relatively static plant than from flow separated at swaying branches. The earlier will be able to strike the bottom mainly at peak-velocity phases where  $L_{exc}$  is the longest and if plant excursions scales with the canopy height. Note in flow A negative-bed shear stress increasings at  $\theta = 270^\circ$ , where plant excursion and oscillation excursion are

the maximum ( $A = 54 \text{ mm}$  and  $L_{\text{exc}} = 94$  and  $105 \text{ mm}$ ). This may be attributed to flow separating from the deflected plant and disrupting the near-bottom velocity distribution i.e. altering bed shear stress distribution. Pan et al. [47] explain that larger plant excursion leads to strong vortex shedding towards to bed. Later quadrant analysis shows sudden increase of Q1 events at  $270^\circ$  corresponding to events that move low momentum flow from lower elevation to higher elevations in the negative-velocity part of the oscillation and coinciding with potentially flow separated from deflected branches.

We notice that the heterogeneity of the plant morphology, and its behavior as it sways in response to the flow, can create areas of stress that differ from spatially averaged estimates, and can bias estimation of sediment transport.

### 3.3 Turbulence

#### 3.3.1 Phase-spatial development of TKE

Phase-averaged values allow us to estimate mean effects on bed stresses, but do not provide enough information regarding large instantaneous bursts and turbulent features. Figure 19 presents phase-variation of the near-bed turbulent kinetic energy (TKE) distribution in the  $y$ -direction past the plant. The inset in Fig. 19 shows the region over which TKE is averaged in  $x$  and  $z$ . Vegetation density (above-ground biomass per unit area) has been found positively correlated with TKE [44]. Studies on arrays of rigid cylinders showing a clear increase of TKE as array density increases [61, 62], but flexible vegetation canopies are associated with a reduction in TKE; e.g., [52, 55]. Our single-plant cases represent an

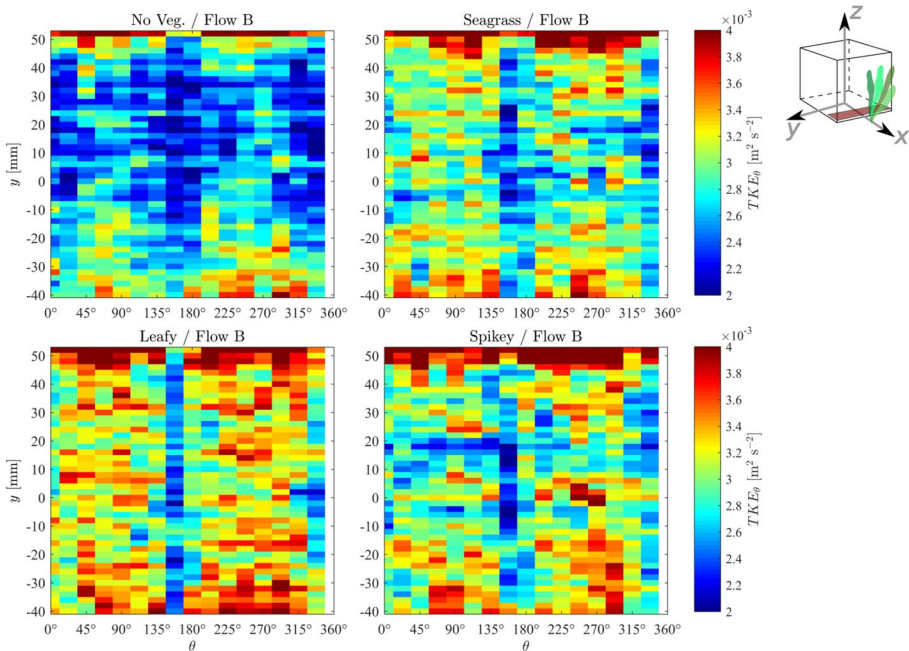


**Fig. 19** Transverse distribution of phase-averaged TKE at  $z = 2 \text{ mm}$ , past the plant as shown in the inset, for flow condition B,  $T = 5 \text{ s}$  and  $A = 54 \text{ mm}$ , for all plant types studied

extremely sparse condition, where near-bed TKE is enhanced not by the combined TKE generated by an array, but by flow perturbations generated by a single swaying plant. The variations in TKE are consistent with Tempest et al. [59], who pointed out that high TKE and local scouring is found in salt marsh canopies around isolated plants or small vegetation patches.

Our data show that: (a) a clear increase in TKE driven by the presence of the different plants, (b) higher TKE levels for spikey and leafy morphology, larger than the generated by the smoother blades from seagrass, (c) a more widely transversely distributed TKE for the leafy plant compared with the spikey plant, corresponding to the lateral,  $y$ -direction, incursions of the leafy morphology, whereas the spikey plant remains mostly constrained in an  $x$ - $z$  plane, (d) higher values are seen for the range  $180^\circ$ – $360^\circ$  than  $0^\circ$ – $180^\circ$ , corresponding to the range on which the plant sways towards the sampling volume, and (e) a maximum found for the spikey case around  $y = 0$  mm,  $\theta = 225^\circ$ – $270^\circ$ , corresponding to the spikey stems getting the closest to the bed within the sampling volume during the maximum flow speed than the other plant types. These observations highlight the need to consider not only the frontal area of plant elements, but their location and orientation at different phases of the flow, to improve prediction schemes of velocity and shear stress in order to more accurately estimate sediment transport.

### 3.3.2 Quadrant events distribution

Figure 20 presents relative frequency of instantaneous turbulent events (represented by combinations of  $u'$  and  $w'$ ), defined as the ratio between the number of events  $N_q$  taking place in the quadrant  $q$  (1, 2, 3, or 4) and the total number of events in all quadrants ( $N_T = N_1 + N_2 + N_3 + N_4$ ) at the  $x$ – $y$  plane located at  $z = 10$  mm and bounded between  $x = 30$  mm and 40 mm. In contrast to phase-averaged velocities, we find that velocity fluctuations are more sensitive to laser reflection from the bottom. Vertical elevation equal to 10 mm is the closest  $z$  elevation where reflections do not introduce excessive noise in velocity fluctuations. Clear patterns of turbulent events are found at this near-bottom elevation. Following a typical quadrant analysis, we examine the occurrence of sweeps ( $u' > 0$ ,  $w' < 0$ , Quadrant 4), ejections ( $u' < 0$ ,  $w' > 0$ , Quadrant 2), outward interactions ( $u' > 0$ ,  $w' > 0$ , Quadrant 1), and inward interactions ( $u' < 0$ ,  $w' < 0$ , Quadrant 3). The number of events identified for each quadrant, divided by the total number of events recorded, yield the percentages shown in Fig. 20. Flow is dominated by outward and sweeps events over the positive-velocity phases, while over the negative-velocity phases, inward and ejection events dominate. Vegetation enhance the occurrence of the ( $u'$ ,  $w'$ ) fluctuation events. Yang and Choi [69] found that sweep interactions are more frequent in vegetated flows near the bottom. An increasing frequency of fluctuation events near the bottom suggest higher potential for sediment resuspension [57]. By combining sweep-outward and ejection-inward interactions, turbulent fluctuations can pick sediment particles up at the bottom and bring them into suspension. Even for a single plant, a clear increase in prevalence of these turbulent events is noticed in comparison with the non-vegetated scenario. Frequency of these instantaneous turbulent events varies with plant morphology. We notice a larger effect by spikey and leafy morphologies, which for the present study have a wider range of motion during a wave period, have multiple scales at which wakes can be generated (spines/leaves, crowns, stems) and reach a closer proximity to the bed when swaying towards the sampling volume, in contrast with the smoother blades of the seagrass type. Even if the seagrass would show a larger frontal area when considering all blades, the

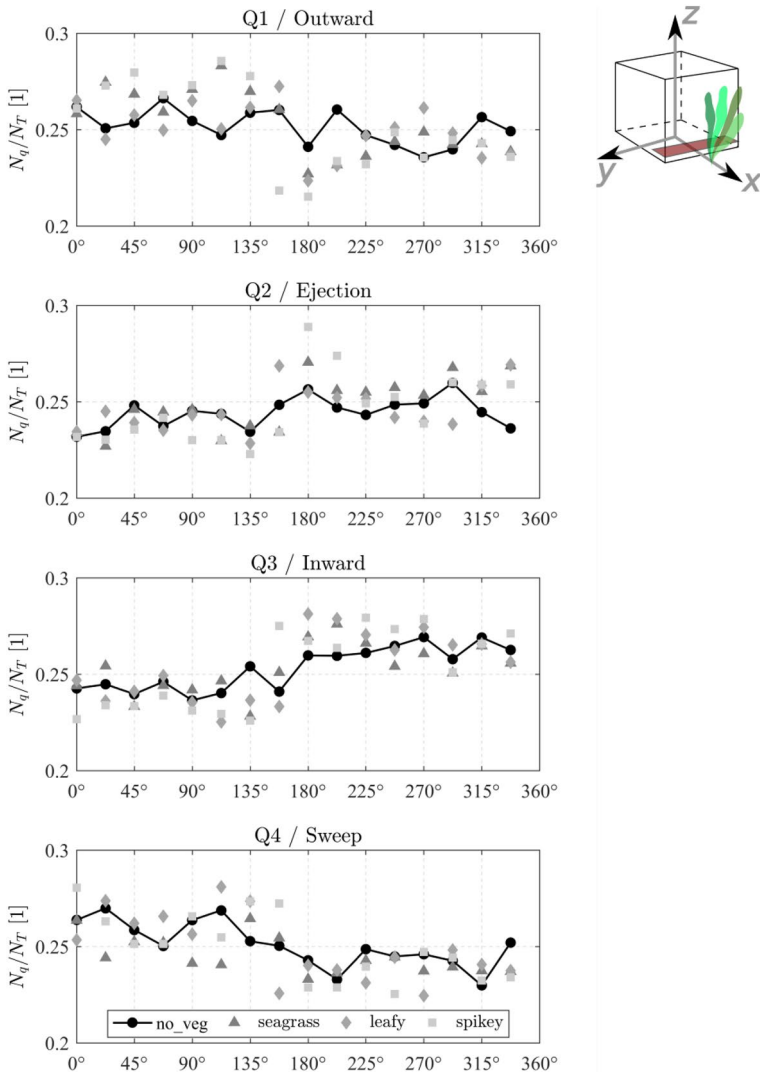


**Fig. 20** Proportion of  $(u', w')$  events occurring at each quadrant of the  $u' - w'$  plane at  $z = 10$  mm, past the plant as shown in the inset, for flow condition B,  $T = 5$  s and  $A = 54$  mm, for all plant types studied

alignment with respect to the flow allows for a smaller effect in TKE generation than the thinner, more complex geometry of the spikey and leafy plants.

### 4 Conclusions

Studies on aquatic vegetation often characterize the effect of vegetation patches in terms of their porosity, frontal area, height, submergence ratio, and population density. Such parameters are used to classify them as “sparse” or “dense” arrays, a designation that specifies



whether they can prevent or enhance bed stresses and thus sediment transport within the patches. Our study explored the lowest end of vegetation density, conducted with a single submerged plant, to explore the effect of three different plant morphologies, representative of vegetation on riverine, tidal, and coastal conditions. The study, using a 3D-volumetric PIV system, found differences among the three vegetation species in the recorded magnitude, as well as temporal and spatial distributions, of bed shear stresses, turbulent kinetic energy, and instantaneous turbulent events. Such changes were associated not only with the plant morphology (blades, leaves, or needles), but also the relative position and orientation with respect to the flow, as different plants can sway around their  $x$ ,  $y$ , or  $z$  axis throughout the oscillation period depending on their morphology, with some species bending to a closer proximity to the bed, allowing for blade- and leave-scale eddies from the prone branches to interact with the bed. Even though this study do not seek to formulate a sediment transport relationship, it suggests that, at the limit of extreme sparse flexible canopy, morphology and biomechanical characteristics influence the local near-bed turbulence and surrounding flow structure under oscillatory conditions. Studies have shown that sparse vegetation have little impact on the bulk flow structure, acting only as flow roughness and producing turbulence at the stem-scale in unidirectional settings. This works explores further into how even a single flexible plant, as it bends with the flow, can locally alter flow organization and turbulence, enough to alter bed shear stress and instantaneous turbulent events to potentially enhance sediment transport even within the sparsest flexible canopies. Our study also shows that such an effect can be quantified by identifying correlations between oscillation period and plant excursion with morphological parameters of the vegetation. In addition, we show that characterizing plants with a single porosity or plant density parameter can neglect significant instantaneous turbulent events, such that the range of motion of the plant under study must be considered to quantify a range of stress and turbulence values that can be generated even within very sparse patches of vegetation, in order to improve predictions of erosion and deposition patterns within them.

**Acknowledgements** JS was supported by UIUC-CEE Departmental Funds. GVC was supported by the SROP at UIUC. Data presented in this manuscript are available through Figshare at <https://doi.org/10.6084/m9.figshare.7794011.v1>.

## References

1. Abdolahpour M, Ghisalberti M, Lavery P, McMahon K (2017) Vertical mixing in coastal canopies. *Limnol Oceanogr* 62(1):26–42
2. Abdolahpour M, Ghisalberti M, McMahon K, Lavery PS (2018) The impact of flexibility on flow, turbulence, and vertical mixing in coastal canopies. *Limnol Oceanogr* 63(6):2777–2792
3. Abdolahpour M, Hambleton M, Ghisalberti M (2017) The wave-driven current in coastal canopies. *J Geophys Res Oceans* 122(5):3660–3674
4. Aberle J, Järvelä J (2015) Hydrodynamics of vegetated channels. In: Rowiński P, Radecki-Pawlik A (eds) *Rivers—physical, fluvial and environmental processes*. Cham, Switzerland, pp 519–541
5. Albayrak I, Nikora V, Miler O, O’Hare MT (2014) Flow-plant interactions at leaf, stem and shoot scales: drag, turbulence, and biomechanics. *Aquat Sci* 76(2):269–294
6. Anderson ME, Smith JM (2014) Wave attenuation by flexible, idealized salt marsh vegetation. *Coast Eng* 83:82–92
7. Boothroyd RJ, Hardy RJ, Warburton J, Marjoribanks TI (2016) The importance of accurately representing submerged vegetation morphology in the numerical prediction of complex river flow. *Earth Surf Process Landf* 41(4):567–576
8. Bornette G, Puijalón S (2011) Response of aquatic plants to abiotic factors: a review. *Aquat Sci* 73(1):1–14

9. Carstensen S, Sumer BM, Fredsøe J (2010) Coherent structures in wave boundary layers. Part 1. Oscillatory motion. *J Fluid Mech* 646:169–206
10. Chang K, Constantinescu G (2015) Numerical investigation of flow and turbulence structure through and around a circular array of rigid cylinders. *J Fluid Mech* 776:161–199
11. Flammang BE, Lauder GV, Troolin DR, Strand TE (2011) Volumetric imaging of fish locomotion. *Biol Lett* 7(5):695–698
12. García MH, López F, Dunn C, Alonso CV (2004) Flow, turbulence, and resistance in a flume with simulated vegetation. In: Bennett SJ, Simon A (eds) *Riparian vegetation and fluvial geomorphology*. American Geophysical Union, Washington, pp 11–27
13. Ghisalberti M, Nepf HM (2002) Mixing layers and coherent structures in vegetated aquatic flows. *J Geophys Res Oceans* 107(C2):3-1–3-11
14. Ghisalberti M, Schlosser T (2013) Vortex generation in oscillatory canopy flow. *J Geophys Res Oceans* 118(3):1534–1542
15. Guilmineau E, Queutey P (2002) A numerical simulation of vortex shedding from an oscillating circular cylinder. *J Fluids Struct* 16(6):773–794
16. Hansen JC, Reidenbach MA (2012) Wave and tidally driven flows in eelgrass beds and their effect on sediment suspension. *Mar Ecol Prog Ser* 448:271–288
17. Hansen JC, Reidenbach MA (2017) Turbulent mixing and fluid transport within florida bay seagrass meadows. *Adv Water Resour* 108:205–215
18. Henriquez M, Reniers A, Ruessink B, Stive M (2012) Vortex tubes in the wave bottom boundary layer. In: Wouter Kranenburg EH, Wijnberg KM (eds) *Proceedings of the 6th European conference on computer systems*. University of Twente, Department of Water Engineering & Management, pp 143–146
19. Henry PY, Myrhaug D, Aberle J (2015) Drag forces on aquatic plants in nonlinear random waves plus current. *Estuar Coast Shelf Sci* 165:10–24
20. Heuner M, Silinski A, Schoelynck J, Bouma TJ, Puijalon S, Troch P, Fuchs E, Schröder B, Schröder U, Meire P et al (2015) Ecosystem engineering by plants on wave-exposed intertidal flats is governed by relationships between effect and response traits. *PLoS ONE* 10(9):e0138086
21. Hino M, Kashiwayanagi M, Nakayama A, Hara T (1983) Experiments on the turbulence statistics and the structure of a reciprocating oscillatory flow. *J Fluid Mech* 131:363–400
22. Horstman EM, Bryan KR, Mullarney JC, Pilditch CA, Eager CA (2018) Are flow-vegetation interactions well represented by mimics? A case study of mangrove pneumatophores. *Adv Water Resour* 111:360–371
23. Jensen B, Sumer B, Fredsøe J (1989) Turbulent oscillatory boundary layers at high reynolds numbers. *J Fluid Mech* 206:265–297
24. Kilminster K, McMahon K, Waycott M, Kendrick GA, Scanes P, McKenzie L, O'Brien KR, Lyons M, Ferguson A, Maxwell P et al (2015) Unravelling complexity in seagrass systems for management: Australia as a microcosm. *Sci Total Environ* 534:97–109
25. Kuo J, Den Hartog C (2007) Seagrass morphology, anatomy, and ultrastructure. In: Larkum AWD, Orth RJ, Duarte CM (eds) *Seagrasses: biology, ecology and conservation*. Springer, Dordrecht, pp 51–87
26. Lauder GV, Flammang B, Alben S (2012) Passive robotic models of propulsion by the bodies and caudal fins of fish. *Integr Comp Biol* 52(5):576–587
27. Lee SY, Primavera JH, Dahdouh-Guebas F, McKee K, Bosire JO, Cannicci S, Diele K, Fromard F, Koedam N, Marchand C et al (2014) Ecological role and services of tropical mangrove ecosystems: a reassessment. *Glob Ecol Biogeogr* 23(7):726–743
28. Lehn AM, Colin SP, Costello JH, Leftwich MC, Tytell ED (2015) Volumetric flow around a swimming lamprey. In: *APS meeting Abstracts*
29. Liénard J, Lynn K, Strigul N, Norris BK, Gatzliolis D, Mullarney JC, Karin RB, Henderson SM (2016) Efficient three-dimensional reconstruction of aquatic vegetation geometry: estimating morphological parameters influencing hydrodynamic drag. *Estuar Coast Shelf Sci* 178:77–85
30. Losada IJ, Maza M, Lara JL (2016) A new formulation for vegetation-induced damping under combined waves and currents. *Coast Eng* 107:1–13
31. Lowe RJ, Koseff JR, Monismith SG (2005) Oscillatory flow through submerged canopies: 1. Velocity structure. *J Geophys Res Oceans* 110(C10016):1–17
32. Luhar M, Nepf H (2016) Wave-induced dynamics of flexible blades. *J Fluids Struct* 61:20–41
33. Luhar M, Nepf HM (2011) Flow-induced reconfiguration of buoyant and flexible aquatic vegetation. *Limnol Oceanogr* 56(6):2003–2017
34. Luhar M, Rominger J, Nepf H (2008) Interaction between flow, transport and vegetation spatial structure. *Environ Fluid Mech* 8(5–6):423

35. Maxwell PS, Eklöf JS, van Katwijk MM, O'Brien KR, de la Torre-Castro M, Boström C, Bouma TJ, Krause-Jensen D, Unsworth RK, van Tussenbroek BI et al (2017) The fundamental role of ecological feedback mechanisms for the adaptive management of seagrass ecosystems—a review. *Biol Rev* 92(3):1521–1538
36. Maza M, Lara JL, Losada IJ (2015) Tsunami wave interaction with mangrove forests: a 3-d numerical approach. *Coast Eng* 98:33–54
37. Maza M, Lara JL, Losada IJ (2016) Solitary wave attenuation by vegetation patches. *Adv Water Resour* 98:159–172
38. Mujal-Colilles A, Christensen KT, Bateman A, Garcia MH (2016) Coherent structures in oscillatory flows within the laminar-to-turbulent transition regime for smooth and rough walls. *J Hydraul Res* 54(5):502–515
39. Mujal-Colilles A, Mier JM, Christensen KT, Bateman A, Garcia MH (2014) Piv experiments in rough-wall, laminar-to-turbulent, oscillatory boundary-layer flows. *Exp Fluids* 55(1):1633
40. Mullarney JC, Henderson SM, Reynolds JA, Norris BK, Bryan KR (2017) Spatially varying drag within a wave-exposed mangrove forest and on the adjacent tidal flat. *Cont Shelf Res* 147:102–113
41. Nepf H (1999) Drag, turbulence, and diffusion in flow through emergent vegetation. *Water Resour Res* 35(2):479–489
42. Nepf HM (2012) Flow and transport in regions with aquatic vegetation. *Annu Rev Fluid Mech* 44:123–142
43. Nielsen P (1992) Coastal bottom boundary layers and sediment transport, vol 4. World Scientific Publishing Company, Singapore
44. Norris BK, Mullarney JC, Bryan KR, Henderson SM (2017) The effect of pneumatophore density on turbulence: a field study in a sonneratia-dominated mangrove forest, vietnam. *Cont Shelf Res* 147:114–127
45. O'Hare MT, Aguiar FC, Asaeda T, Bakker ES, Chambers PA, Clayton JS, Elger A, Ferreira TM, Gross EM, Gunn ID et al (2017) Plants in aquatic ecosystems: current trends and future directions. *Hydrobiologia* 812(1):1–11
46. Ortiz AC, Ashton A, Nepf H (2013) Mean and turbulent velocity fields near rigid and flexible plants and the implications for deposition. *J Geophys Res Earth Surf* 118(4):2585–2599
47. Pan Y, Follett E, Chamecki M, Nepf H (2014) Strong and weak, unsteady reconfiguration and its impact on turbulence structure within plant canopies. *Phys Fluids* 26(10):2003–2017
48. Patterson MR, Harwell MC, Orth LM, Orth RJ (2001) Biomechanical properties of the reproductive shoots of eelgrass. *Aquat Bot* 69(1):27–40
49. Paul M, Henry PY, Thomas R (2014) Geometrical and mechanical properties of four species of northern european brown macroalgae. *Coast Eng* 84:73–80
50. Pope SB (2000) Turbulent flows. Cambridge University Press, Cambridge
51. Pothos S, Troolin D, Lai W, Menon R (2009) V3v-volumetric three-component velocimetry for 3d flow measurements main principle, theory and applications. *Rev Termotec* 2:2009
52. Pujol D, Casamitjana X, Serra T, Colomer J (2013) Canopy-scale turbulence under oscillatory flow. *Cont Shelf Res* 66:9–18
53. Pujol D, Serra T, Colomer J, Casamitjana X (2013) Flow structure in canopy models dominated by progressive waves. *J Hydrol* 486:281–292
54. Reidenbach MA, Monismith SG, Koseff JR, Yahel G, Genin A (2006) Boundary layer turbulence and flow structure over a fringing coral reef. *Limnol Oceanogr* 51(5):1956–1968
55. Ros À, Colomer J, Serra T, Pujol D, Soler M, Casamitjana X (2014) Experimental observations on sediment resuspension within submerged model canopies under oscillatory flow. *Cont Shelf Res* 91:220–231
56. Schnauder I, Moggridge HL (2009) Vegetation and hydraulic-morphological interactions at the individual plant, patch and channel scale. *Aquat Sci* 71(3):318
57. Sterk G, Jacobs A, Van Boxel J et al (1998) The effect of turbulent flow structures on saltation sand transport in the atmospheric boundary layer. *Earth Surf Process Landf* 23(10):877–887
58. Tanino Y, Nepf HM (2008) Lateral dispersion in random cylinder arrays at high reynolds number. *J Fluid Mech* 600:339–371
59. Tempest JA, Möller I, Spencer T (2015) A review of plant-flow interactions on salt marshes: the importance of vegetation structure and plant mechanical characteristics. *Wiley Interdiscip Rev Water* 2(6):669–681
60. Tinoco R, Coco G (2014) Observations of the effect of emergent vegetation on sediment resuspension under unidirectional currents and waves. *Earth Surf Dyn* 2(1):83
61. Tinoco R, Coco G (2018) Turbulence as the main driver of resuspension in oscillatory flow through vegetation. *J Geophys Res Earth Surf* 123(5):891–904

62. Tinoco RO, Coco G (2016) A laboratory study on sediment resuspension within arrays of rigid cylinders. *Adv Water Resour* 92:1–9
63. Tinoco RO, Cowen EA (2013) The direct and indirect measurement of boundary stress and drag on individual and complex arrays of elements. *Exp Fluids* 54(4):1509
64. Vittori G, Verzicco R (1998) Direct simulation of transition in an oscillatory boundary layer. *J Fluid Mech* 371:207–232
65. Wang X, Xie W, Zhang D, He Q (2016) Wave and vegetation effects on flow and suspended sediment characteristics: a flume study. *Estuar Coast Shelf Sci* 182:1–11
66. Wilson CJ, Wilson PS, Greene CA, Dunton KH (2010) Seagrass leaves in 3-d: using computed tomography and low-frequency acoustics to investigate the material properties of seagrass tissue. *J Exp Mar Biol Ecol* 395(1–2):128–134
67. Wu WC, Cox DT (2015) Effects of wave steepness and relative water depth on wave attenuation by emergent vegetation. *Estuar Coast Shelf Sci* 164:443–450
68. Yang JQ, Kerger F, Nepf HM (2015) Estimation of the bed shear stress in vegetated and bare channels with smooth beds. *Water Resour Res* 51(5):3647–3663
69. Yang W, Choi SU (2009) Impact of stem flexibility on mean flow and turbulence structure in depth-limited open channel flows with submerged vegetation. *J Hydraul Res* 47(4):445–454
70. Zeller RB, Weitzman JS, Abbett ME, Zarama FJ, Fringer OB, Koseff JR (2014) Improved parameterization of seagrass blade dynamics and wave attenuation based on numerical and laboratory experiments. *Limnol Oceanogr* 59(1):251–266
71. Zhang Y, Tang C, Nepf H (2018) Turbulent kinetic energy in submerged model canopies under oscillatory flow. *Water Resour Res* 54(3):1734–1750

**Publisher's Note** Springer Nature remains neutral with regard to jurisdictional claims in published maps and institutional affiliations.